



EXPERIMENTAL AND NUMERICAL ANALYSES OF FLOW-LIMITED CHEMICAL REACTIONS IN LAMINAR AND TURBULENT REGIMES.

Irene Sancho Conde

Dipòsit Legal: T 994-2015

ADVERTIMENT. L'accés als continguts d'aquesta tesi doctoral i la seva utilització ha de respectar els drets de la persona autora. Pot ser utilitzada per a consulta o estudi personal, així com en activitats o materials d'investigació i docència en els termes establerts a l'art. 32 del Text Refós de la Llei de Propietat Intel·lectual (RDL 1/1996). Per altres utilitzacions es requereix l'autorització prèvia i expressa de la persona autora. En qualsevol cas, en la utilització dels seus continguts caldrà indicar de forma clara el nom i cognoms de la persona autora i el títol de la tesi doctoral. No s'autoritza la seva reproducció o altres formes d'explotació efectuades amb finalitats de lucre ni la seva comunicació pública des d'un lloc aliè al servei TDX. Tampoc s'autoritza la presentació del seu contingut en una finestra o marc aliè a TDX (framing). Aquesta reserva de drets afecta tant als continguts de la tesi com als seus resums i índexs.

ADVERTENCIA. El acceso a los contenidos de esta tesis doctoral y su utilización debe respetar los derechos de la persona autora. Puede ser utilizada para consulta o estudio personal, así como en actividades o materiales de investigación y docencia en los términos establecidos en el art. 32 del Texto Refundido de la Ley de Propiedad Intelectual (RDL 1/1996). Para otros usos se requiere la autorización previa y expresa de la persona autora. En cualquier caso, en la utilización de sus contenidos se deberá indicar de forma clara el nombre y apellidos de la persona autora y el título de la tesis doctoral. No se autoriza su reproducción u otras formas de explotación efectuadas con fines lucrativos ni su comunicación pública desde un sitio ajeno al servicio TDR. Tampoco se autoriza la presentación de su contenido en una ventana o marco ajeno a TDR (framing). Esta reserva de derechos afecta tanto al contenido de la tesis como a sus resúmenes e índices.

WARNING. Access to the contents of this doctoral thesis and its use must respect the rights of the author. It can be used for reference or private study, as well as research and learning activities or materials in the terms established by the 32nd article of the Spanish Consolidated Copyright Act (RDL 1/1996). Express and previous authorization of the author is required for any other uses. In any case, when using its content, full name of the author and title of the thesis must be clearly indicated. Reproduction or other forms of for profit use or public communication from outside TDX service is not allowed. Presentation of its content in a window or frame external to TDX (framing) is not authorized either. These rights affect both the content of the thesis and its abstracts and indexes.

Doctoral Thesis

Irene Sancho Conde

EXPERIMENTAL AND NUMERICAL
ANALYSES OF FLOW-LIMITED CHEMICAL
REACTIONS IN LAMINAR AND TURBULENT
REGIMES

Department of Mechanical Engineering



UNIVERSITAT ROVIRA I VIRGILI

UNIVERSITAT ROVIRA I VIRGILI

EXPERIMENTAL AND NUMERICAL ANALYSES OF FLOW-LIMITED CHEMICAL REACTIONS IN LAMINAR AND
TURBULENT REGIMES.

Irene Sancho Conde

Dipòsit Legal: T 994-2015

UNIVERSITAT ROVIRA I VIRGILI

EXPERIMENTAL AND NUMERICAL ANALYSES OF FLOW-LIMITED CHEMICAL REACTIONS IN LAMINAR AND
TURBULENT REGIMES.

Irene Sancho Conde

Dipòsit Legal: T 994-2015

UNIVERSITAT ROVIRA I VIRGILI

EXPERIMENTAL AND NUMERICAL ANALYSES OF FLOW-LIMITED CHEMICAL REACTIONS IN LAMINAR AND
TURBULENT REGIMES.

Irene Sancho Conde

Dipòsit Legal: T 994-2015

Irene Sancho Conde

EXPERIMENTAL AND NUMERICAL
ANALYSES OF FLOW-LIMITED CHEMICAL
REACTIONS IN LAMINAR AND TURBULENT
REGIMES

Doctoral Thesis

Supervised by:
Dr. Jordi Pallarès
Dr. Anton Vernet

Department of Mechanical Engineering

Tarragona 2015



UNIVERSITAT ROVIRA I VIRGILI

EXPERIMENTAL AND NUMERICAL ANALYSES OF FLOW-LIMITED CHEMICAL REACTIONS IN LAMINAR AND
TURBULENT REGIMES.

Irene Sancho Conde

Dipòsit Legal: T 994-2015



UNIVERSITAT
ROVIRA I VIRGILI

DEPARTAMENT D'ENGINYERIA MECÀNICA

Escola Tècnica Superior d'Enginyeria Química (ETSEQ).
Av. Països Catalans 26. 43007 Tarragona (Spain)

Dr. Jordi Pallarès and Dr. Anton Vernet, Professors of the
Mechanical Engineering Department of Universitat Rovira i Virgili,

CERTIFY:

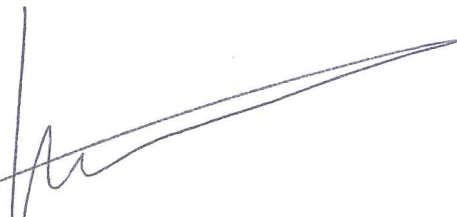
That the present study, entitled:

*Experimental and Numerical Analyses of Flow-Limited Chemical
Reactions in Laminar and Turbulent Regimes*

presented by Mrs Irene Sancho Conde for the award of the degree
of Doctor, has been carried out under our supervision at the
Department of Mechanical Engineering of this university and that it
fulfils all the requirements to be eligible for the European Mention
Award.

And, to inform you of that and in order for it to have the needed
effects, we sign this certification.

Tarragona, April 2015



Dr. Jordi Pallarès



Dr. Anton Vernet

UNIVERSITAT ROVIRA I VIRGILI

EXPERIMENTAL AND NUMERICAL ANALYSES OF FLOW-LIMITED CHEMICAL REACTIONS IN LAMINAR AND
TURBULENT REGIMES.

Irene Sancho Conde

Dipòsit Legal: T 994-2015

UNIVERSITAT ROVIRA I VIRGILI

EXPERIMENTAL AND NUMERICAL ANALYSES OF FLOW-LIMITED CHEMICAL REACTIONS IN LAMINAR AND
TURBULENT REGIMES.

Irene Sancho Conde

Dipòsit Legal: T 994-2015

A mi padre

UNIVERSITAT ROVIRA I VIRGILI

EXPERIMENTAL AND NUMERICAL ANALYSES OF FLOW-LIMITED CHEMICAL REACTIONS IN LAMINAR AND
TURBULENT REGIMES.

Irene Sancho Conde

Dipòsit Legal: T 994-2015

Index

Abstract.....	v
Resumen	ix
Agradecimientos	xiii
List of Publications and Conferences	xv
Internship	xvii
List of Tables	xix
List of Figures.....	xxi
List of Symbols.....	xxix
0. Objectives	1
1. Introduction	3
2. Chemical Reaction in a Plane Turbulent Channel Flow.....	13
2.1. Physical and Mathematical Model	13
2.2. Mixing Contribution	17
2.3. Analysis of the Flow Structures	24
2.4. Conclusions	30

3. Chemical Reaction in a Confined Laminar Flow	33
3.1. Experimental Setup	33
3.1.1. Light Source and Image Acquisition	36
3.2. Experimental Techniques	37
3.2.1. Particle Image Velocimetry Technique	37
3.2.2. Planar Laser Induced Fluorescence Technique	42
3.2.3. Simultaneous PIV and PLIF Techniques	44
3.3. Numerical Simulation	49
3.3.1. Mesh Independence Test	50
3.3.2. Time Step Independence Test	53
3.3.3. Acid Solution Inlet Analysis	53
3.4. Flow Stabilization Time	54
3.5. Velocity Measurements	55
3.6. Simultaneous Velocity and Concentration Measurements ..	61
3.7. Conclusions	71
4. Particle Deposition on the Wall of a Microchannel for Enzymatic Reactions	75
4.1. Experimental Setup	75

4.2. Numerical Simulation.....	78
4.2.1. Mesh Independence Test	83
4.3. Results	85
4.3.1. Experimental Results.....	85
4.3.2. Numerical Results	87
4.3.3. Comparison between Experimental and Numerical Results	88
4.4. Conclusions	89
References	91

Abstract

The main goal of this thesis is to analyse, experimentally and numerically, the effect of the flow in different chemical reactions. This thesis is divided in three big blocks where different flow regimes are analysed.

Turbulent mixing has the ability to transport and mix chemical species, energy, and momentum faster than molecular diffusion and, consequently, it is widely used in industrial chemical processes. For this reason, in the last years, turbulent mixing has been widely studied. In the first block of this thesis, a database obtained from a direct numerical simulation of the turbulent reacting flow in a plane channel at low Reynolds number ($Re_\tau = 180$) is analysed. One reactant is released along a line source at the center of the channel and the other near the walls of the channel. This distribution produces two reacting mass transfer mixing layers. The fluctuations of the concentration of the chemical species that react following a second-order chemical reaction ($Da = 1$, $Sc = 0.7$) are processed to determine the contribution of the large and the small-scale fluctuations in the reacting mass transfer mixing layers. The analysis is extended to educe the flow structures responsible for the large and the small fluctuations of concentration in the mixing layers.

In the second block of this thesis, a reactive flow in laminar regime is analysed. Previous studies have shown that the analyses of concentration fields in turbulent mixing by means of experimental

techniques and numerical simulations are not straightforward and, in some cases, the comparison of results obtained with both approaches are not in good agreement. For this reason, this block analyses, numerically and experimentally, a laminar reactive flow in a cylindrical cavity with a rotating endwall. A basic solution is initially in the cavity and an acid solution is introduced at very low velocity through the center of the stationary endwall when the flow in the cavity is at the steady state. The effect of the different flow structures obtained at different Reynolds numbers on the irreversible fast acid-base neutralization reaction is measured with a simultaneous Particle Image Velocimetry (PIV) and Planar Laser Induced Fluorescence (PLIF) techniques and simulated numerically with a finite volume code. The observed flow structures, the recirculation bubbles in the vortex breakdown regions as well as the numerical velocity profiles are in agreement with the measurements and with previous studies. The range of measured concentrations is limited to regions where the molar fraction of the base is $x_B \geq 0.57$. The comparison between the experimental and numerical contours of concentration of base solution at $Re = 1000$ and 1500 are in general agreement. At larger Reynolds numbers ($Re = 1700, 2000$ and 2300), the experimental and numerical contours of concentration of base solution inside the vortex breakdown bubbles differ because of the relatively large concentration of product (i.e. $x_B < 0.57$) in these regions, which is predicted by the numerical simulations.

The third part of this thesis deals with chemical reactions in microchannels. Specifically, we consider enzymatic reactions in microchannels using magnetic micro-particles. As first step, this third block analyses the rate of deposition of magnetic particles on the walls of microchannel. A permanent magnet is placed out of the channel to induce the deposition of the particles which are introduced at different flow rates. Two types of magnetic particles are analysed; the paramagnetic and superparamagnetic particles. Superparamagnetic particles deposit on the wall in a non-uniform manner. Specifically, they line-up and form parallel chains. On the contrary, paramagnetic particles deposit on the wall forming a convex shape around the area adjacent to the permanent magnet. Additionally, a numerical model to simulate the deposition of the paramagnetic particles is studied and it is observed that, at high flow rates, the experimental and numerical results are consistent. Both experimental and numerical results show that the higher the flow rate the lower the accumulation rate of particles. Finally, it is quantified the number of particles deposited on the wall and it is observed that the deposition rate decreases exponentially with the flow rate. These results open the prospect for further analysis such as the enzymes immobilization in the magnetic beads and its correspondent kinetic enzyme reaction study in the microchannel.

UNIVERSITAT ROVIRA I VIRGILI

EXPERIMENTAL AND NUMERICAL ANALYSES OF FLOW-LIMITED CHEMICAL REACTIONS IN LAMINAR AND
TURBULENT REGIMES.

Irene Sancho Conde

Dipòsit Legal: T 994-2015

Resumen

El objetivo principal de esta tesis es analizar, tanto experimentalmente cómo numéricamente, el efecto del flujo en diferentes reacciones químicas. Esta tesis se divide en tres grandes bloques donde se analizan distintos regímenes de flujo.

La mezcla turbulenta tiene la habilidad de transportar y mezclar especies químicas, energía y momento más rápidamente que por difusión molecular y, como consecuencia, es ampliamente utilizada en procesos químicos industriales. Por esta razón, en los últimos años, la mezcla turbulenta ha sido estudiada extensamente. En el primer bloque de esta tesis se analiza una base de datos, obtenida a partir de simulación numérica directa, de un flujo reactivo y turbulento en un canal a bajo número de Reynolds ($Re_\tau = 180$). Un reactivo es liberado a lo largo del centro del canal, y el otro cerca de las paredes del canal. Esta distribución produce dos capas de mezcla reactiva donde se produce intercambio de materia. Las fluctuaciones de la concentración de las especies químicas, que reaccionan siguiendo una reacción química de segundo orden ($Da = 1$, $Sc = 0.7$), se procesan para determinar la contribución de las fluctuaciones a pequeña y a gran escala en las capas de mezcla reactiva. El análisis se extiende para explicar las estructuras de flujo responsables de las grandes y pequeñas fluctuaciones de la concentración en las capas de mezcla.

En el segundo bloque de esta tesis, se analiza un flujo reactivo en régimen laminar. Estudios previos han mostrado que el análisis de

los campos de concentración en mezclas turbulentas a través de técnicas experimentales y simulaciones numéricas no es trivial y que, en algunos casos, la comparación de los resultados obtenidos con ambos enfoques difieren. Por este motivo, en este bloque se analiza, tanto numéricamente cómo experimentalmente, un flujo reactivo y laminar en una cavidad cilíndrica con la pared superior rotativa. Dentro de la cavidad cilíndrica se encuentra inicialmente la solución básica. La solución ácida se introduce dentro de la cavidad a muy baja velocidad a través del centro de la pared estacionaria inferior cuando el flujo en la cavidad cilíndrica se encuentra en estado estacionario. El efecto de las diferentes estructuras de flujo obtenidas a diferentes números de Reynolds en una reacción irreversible de neutralización ácido-base, se mide utilizando las técnicas experimentales *Particle Image Velocimetry* (PIV) y *Planar Laser Induced Fluorescence* (PLIF), y numéricamente a través de simulaciones que utilizan volúmenes finitos. Se ha observado que las estructuras de flujo, las burbujas de recirculación en las regiones donde hay rompimiento de vórtice como también los perfiles de velocidad numéricos están de acuerdo con los resultados experimentales y con estudios previos. El rango para medir concentraciones se limita a regiones donde la fracción molar de la solución básica es $x_B \geq 0.57$. La comparación entre los contornos experimentales y numéricos de concentración de la solución básica a $Re = 1000$ y 1500 están en concordancia. A números de Reynolds más elevados ($Re = 1700, 2000$ y 2300), los contornos experimentales y numéricos de la concentración de la solución básica dentro de las burbujas del rompimiento de vórtice difieren

debido a que la concentración de producto es relativamente alta (es decir, $x_B < 0.57$) en estas regiones, la cual se predice por simulación numérica.

Para profundizar en el estudio de las reacciones químicas, se da el primer paso para analizar reacciones enzimáticas en microcanales utilizando micro-partículas magnéticas. En el tercer bloque de esta tesis, se analiza la tasa de partículas magnéticas que se depositan en las paredes de un microcanal. Un imán permanente se coloca fuera del canal para inducir la deposición de las partículas que se introducen a diferentes caudales. Se analizan dos tipos de partículas magnéticas, las paramagnéticas y las superparamagnéticas. Las partículas superparamagnéticas se depositan en la pared del microcanal de una manera no uniforme. En concreto, se alinean y forman cadenas paralelas. Por el contrario, las partículas paramagnéticas se depositan formando una forma convexa alrededor de la zona adyacente al imán permanente. Además, se estudia un modelo numérico para simular la deposición de las partículas paramagnéticas y se observa que, a altos caudales, los resultados experimentales y numéricos son consistentes. Ambos resultados numéricos y experimentales muestran que cuanto mayor es el caudal, menor es la acumulación de las partículas magnéticas. Finalmente se cuantifica el número de partículas depositadas en la pared y se observa que la tasa de deposición de las partículas disminuye exponencialmente con el caudal. Estos resultados abren la posibilidad para un análisis adicional tal como la inmovilización

de enzimas en las partículas magnéticas y su correspondiente estudio de la cinética de la reacción enzimática en el microcanal.

Agradecimientos

El trabajo presentado en esta memoria ha sido desarrollado dentro del grupo de investigación *Experiments, Computation and Modelization in Fluid Mechanics and Turbulence* (ECoMMFiT) adscrito al Departamento de Ingeniería Mecánica de la *Escola Tècnica Superior d'Enginyeria Química* (ETSEQ) de la Universitat Rovira i Virgili bajo la dirección conjunta de los Drs. Jordi Pallarès y Anton Vernet.

A Jordi y Anton, sin ellos esta tesis no hubiera sido posible. Gracias por vuestra ayuda y por vuestra paciencia y por tener la puerta de vuestros despachos siempre abierta.

A Tiina Sikanen y a Salvatore Cito por su ayuda durante mi estancia en la Universidad de Helsinki. Gracias por darme la oportunidad de entrar en el mundo de los microcanales y por hacerme sentir como si estuviera en casa.

A todos mis compañeros del ECoMMFiT, a los que siguen en él y a los que ya se fueron. Sobretudo agradecer al *Ilustrísimo Club de Caballeros*, David, Albert, Javi y Valentín. El doctorado no hubiera sido lo mismo sin vosotros, por los momentos que hemos pasado dentro y sobre todo fuera de la universidad.

A Yolanda, por nuestras innumerables charlas en los pasillos. Este último año te he echado mucho de menos. A Maria “la Serralenca” que aunque no fueras del grupo, no sabemos cómo no te perdías ningún sarao. A Noemí, por ser mi compañera de los miércoles.

A mi madre por su continuo apoyo y paciencia. A Hèctor, Tatiana, Mireia, Joan y Aloma por estar siempre conmigo. Y sobre todo a Valentín, sin ti el doctorado no hubiera sido lo mismo, gracias por apoyarme en los buenos y en los malos momentos. Te quiero.

Finalmente agradecer el soporte financiero concebido por la *Generalitat de Catalunya* al otorgarme la beca 2012FI_B 00535.

Nada más me queda por agradecer a los miembros del tribunal por aceptar juzgar esta tesis doctoral y a todas las personas que, directa o indirectamente, han participado en su elaboración.

List of Publications and Conferences

Publications in Journal Papers

I. Sancho, A. Fabregat, J. Pallares, A. Vernet. “Macro- and micromixing in a plane turbulent channel flow with a second-order chemical reaction” *Computers and Fluids*, 2013, 88, 156-164.

I. Sancho, S. Varela, J. Pallares, A. Vernet. “Characterization of the reacting laminar flow in a cylindrical cavity with a rotating endwall using numerical simulations and a combined PIV/PLIF technique” *International Journal of Heat and Mass Transfer* (Submitted March 2015).

Contribution to Conferences

I. Sancho, A. Fabregat, J. Pallares, A. Vernet, “Second-order chemical reaction micro- and macro-mixing in a plane turbulent channel”, 7th International Symposium on Turbulence, Heat and Mass Transfer, Palermo (Italy), September 2012. Poster presentation.

I. Sancho, S. Varela, J. Pallares, A. Vernet, “Simultaneous PLIF and PIV measurements of a confined laminar reactive flow in a cylindrical cavity”, 10th International Symposium on Particle Image Velocimetry, Delft (Netherlands), July 2013. Oral presentation.

I. Sancho, S. Varela, J. Pallares, A. Vernet, “Analysis of a confined laminar reactive flow in a cylindrical cavity using PLIF and PIV”,

7th Workshop on Research in Turbulence and Transition, Terrassa
(Spain), October 2013. Oral presentation.

I. Sancho, S. Varela, J. Pallares, A. Vernet, “Analysis of a confined
laminar reactive flow in a cylindrical cavity using PLIF and PIV”,
11th Doctoral Day Poster Exhibition, Tarragona (Spain), April 2014.

I. Sancho, S. Varela, J. Pallares, A. Vernet, “Combined PLIF/PIV
measurements of a confined laminar reactive flow in a cylindrical
cavity”, 17th International Symposium on Applications of Laser
Techniques to Fluid Mechanics, Lisbon (Portugal), July 2014. Oral
presentation.

Internship

University of Helsinki - European Mention

28th July 2014 to 31st October 2014

Advisor: Tiina Sikanen

Development of experimental and numerical methods based on the microfabrication and microfluidics to analyse the magnetic particles deposition rate on the walls of a microchannel and open the prospect for further analysis such as the enzymes immobilization in the magnetic beads.

UNIVERSITAT ROVIRA I VIRGILI

EXPERIMENTAL AND NUMERICAL ANALYSES OF FLOW-LIMITED CHEMICAL REACTIONS IN LAMINAR AND
TURBULENT REGIMES.

Irene Sancho Conde

Dipòsit Legal: T 994-2015

List of Tables

Table 3.1. Boundary layers (BL) parameters.	51
Table 4.1. Properties of magnetic particles.	76

List of Figures

Figure 2.1. Schematic representation of the computational domain with dimensions $L_x \times L_y \times L_z = 8\pi\delta \times 2\pi\delta \times 2\delta$. The domain is discretized using a staggered grid with a resolution of $258 \times 130 \times 130$ control volumes.....	14
Figure 2.2. Time-evolution of a) fluctuations of the dimensionless concentration of A , b) large-scale fluctuations of the dimensionless concentration of A and c) small-scale fluctuations of the dimensionless concentration of A at $x^* = 4.8$, $y^* = 0$ and $z^* = 0.25$	18
Figure 2.3. Spectra of signals shown in Figure 2.2. The cutting frequency used for the separation is $f \approx 15 u_r/\delta$	19
Figure 2.4. Variance of concentration of A normalized with $\sigma^2 / [\overline{C_A^*}(1 - \overline{C_A^*})]$. a) At the centerline of the channel ($z^* = 0$) and b) near the interface of the concentration mixing layer ($z^* = 0.25$)... ..	21
Figure 2.5. Mixing contribution of reactive scalars at the centerline ($z^* = 0$).	22
Figure 2.6. a) Time-averaged concentration at the centerline ($z^* = 0$) of reactive scalar A and non-reactive scalar (T). b) Mixing contribution of A and T	23
Figure 2.7. Steps of the conditional sampling procedure.	25

Figure 2.8. Conditionally sampled flow responsible for the large-scale fluctuations of A . Flow topology A in terms of the isosurface $\lambda_2 / \text{Min}(\lambda_2) = -0.39$. a) 3D view and b) top view.	26
Figure 2.9. Side view of the flow topology shown in Figure 2.8. Contours of the dimensionless large-scale fluctuations of a) reactive scalar A and b) reactive scalar C	28
Figure 2.10. Contours of the dimensionless small-scale fluctuations of a) reactive scalar A and b) reactive scalar C	29
Figure 3.1. Sketch of the experimental setup.	34
Figure 3.2. a) Picture of cylindrical cavity and rectangular box. b) Picture of the experimental setup.	36
Figure 3.3. Sketch of Particle Image Velocimetry (PIV) arrangement.	38
Figure 3.4. Conceptual arrangement of Particle Image Velocimetry (PIV) technique.	39
Figure 3.5. Sketch of the experimental setup of PIV experiments.	40
Figure 3.6. Images captured during PIV experiments at $Re = 2000$. a) Colour digital camera and b) PIV camera.	41
Figure 3.7. Absorption and emission wavelength of rhodamine B.	41
Figure 3.8. Absorption and emission wavelength of sodium fluorescein.	43

Figure 3.9. Sketch of the experimental setup of simultaneous PIV/PLIF experiments.....	44
Figure 3.10. Calibration of PLIF technique. a) Titration of acid solution + dye in a base solution. b) pH of the solution during the titration.	46
Figure 3.11. Absorption and emission wavelength of rhodamine (RHO) and sodium fluorescein (SF) dyes with the 550 nm filter. .	47
Figure 3.12. PIV and PLIF images at $Re = 1000$ and $t = 10$ min. a) Original PIV image with particles and signal of sodium fluorescein dye. b) Original PLIF image, with some particles. c) Treated PIV image, after post-processing. d) Treated PLIF image clean of particles and with only sodium fluorescein dye.	48
Figure 3.13. Sketch of the boundary layers (BL) used in the meshes. There are three zones: the BL along z - direction, the BL in the center of the cylinder and the BL in the top and bottom walls.....	51
Figure 3.14. Mesh independence test at $Re = 2300$. Mesh 1: 0.36 Mnodes, mesh 2: 0.68 Mnodes and mesh 3: 0.92 Mnodes. a) Mesh independence test of velocity profiles along x -axis at $z^* = 0.375$. b) Mesh independence test of base concentration along the height of the cavity at $x^* = 0.750$ and $y^* = 0$	52
Figure 3.15. Time step size (tss) independence test at $Re = 2300$. Concentration of base solution profile (C_B^*) along z -direction at $x^* = 0.750$ and $y^* = 0$	53

Figure 3.16. Analysis of the effect of the bottom inlet at $Re = 1000$. Axial velocity (w^*) at $y^* = 0$ at different z^* positions of the cylindrical cavity 54

Figure 3.17. Analysis of the time required to achieve the steady state at $Re = 1500$ and at $z^* = 0.25$ 55

Figure 3.18. Velocity plots at different Reynolds number a) $Re = 1000$ and b) $Re = 2300$. Experimental and numerical results of the axial velocity (w^*) at the cylinder axis ($x^* = 0$ and $y^* = 0$). c) $Re = 1000$, d) $Re = 1500$, e) $Re = 1700$, f) $Re = 2000$ and g) $Re = 2300$ 57

Figure 3.19. Experimental and numerical axial velocity (w^*) profiles at different axial positions (z^*) of the cylindrical cavity at $y^* = 0$. a) $Re = 1000$, b) $Re = 1500$, c) $Re = 1700$, d) $Re = 2000$ and e) $Re = 2300$ 59

Figure 3.20. The flow in the horizontal plane at $Re = 1500$. a) In-plane velocity fields at $z^* = 0.500$. b) Comparison between numerical results of Fluent and Caffa3d.MB [47] of velocity profiles (v^*) at $z^* = 0.375$ and $y^* = 0$. c) Experimental and numerical velocity profiles (v^*) at different axial positions (z^*) of cylindrical cavity at $y^* = 0$ 60

Figure 3.21. Comparison between only PIV and PIV/PLIF experimental velocity profiles (w^*) at different axial position (z^*) of

the cylindrical cavity at $y^* = 0$ at a) $Re = 1000$, b) $Re = 1500$, c)
 $Re = 1700$, d) $Re = 2000$ and e) $Re = 2300$ 63

Figure 3.22. Experimental and numerical contours of concentration
 of acid (C_A^*), base (C_B^*) and product (C_C^*) solution at center plane
 ($y^* = 0$) at $t = 10$ min at 1) $Re = 1000$, 2) $Re = 1500$,
 3) $Re = 1700$, 4) $Re = 2000$ and 5) $Re = 2300$.
 a-1) to a-5) Numerical contours of concentration of acid solution.
 bn-1) to bn-5) Numerical contours of concentration of base solution.
 be-1) to be-5) Experimental contours of concentration of base
 solution. c-1) to c-5) Numerical contours of concentration of
 product solution. 64

Figure 3.23. Experimental and numerical contours of intensity (I^*)
 at 1) $Re = 1000$, 2) $Re = 1500$, 3) $Re = 1700$, 4) $Re = 2000$ and 5)
 $Re = 2300$. a-1) to a-5) Experimental contours of intensity. b-1) to
 b-5) Numerical contours of intensity..... 67

Figure 3.24. Numerical contours of intensity (I^*) with a lateral
 displacement in the axis of rotation of the top wall at different
 Reynolds numbers, 1) $Re = 2000$ and 2) $Re = 2300$. a-1) and a-2)
 Displacement of $\Delta x/2R = 1.25 \cdot 10^{-2}$. b-1) and b-2) Displacement of
 $\Delta x/2R = 2.50 \cdot 10^{-2}$. c-1) and c-2) Displacement of $\Delta x/2R = 3.75 \cdot 10^{-2}$
 2 68

Figure 3.25. Experimental and numerical velocity profiles (w^*) at
 different axial positions (z^*) at $y^* = 0$ adding a displacement in the
 axis of the rotating wall of 1) $\Delta x/2R = 1.25 \cdot 10^{-2}$,

2) $\Delta x/2R = 2.50 \cdot 10^{-2}$ and 3) $\Delta x/2R = 3.75 \cdot 10^{-2}$ at different Reynolds numbers a) $Re = 2000$ and b) $Re = 2300$ 69

Figure 3.26. Time evolutions of a) the volume averaged nondimensional product concentration ($\overline{C_C^*}$) and of b) the volume averaged standard deviation ($\overline{\sigma}$) of the product concentration. 71

Figure 4.1. Sketch of the experimental setup. The dimensions of the microchannel are $L \times W \times D_m = 4 \cdot 10^{-2} \times 5 \cdot 10^{-4} \times 7 \cdot 10^{-5}$ m... 76

Figure 4.2. Picture of the microchannel with the permanent magnet. 77

Figure 4.3. Sketch of the geometry in COMSOL Multiphysics 4.4. The rectangle represents the microchannel, the square represents the permanent magnet and the disk is the environment, needed to compute the magnetic fields in COMSOL Multiphysics 4.4. 82

Figure 4.4. Mesh independence test at center of the microchannel ($y = 0$ m) along x -direction at $v_{IN} = 0.02381$ m/s. Mesh 1: 59380 nodes, mesh 2: 149590 nodes and mesh 3: 421010 nodes. a) Velocity magnitude. b) Magnetic flux density. 84

Figure 4.5. Images obtained from the experiments with Dynabeads® Carboxylic Acid beads. a) $Q_v = 0.0100$ mL/min. b) $Q_v = 0.0100$ mL/min removing the magnet. 86

Figure 4.6. Images obtained from the experiments with SPHERO™ Carboxyl magnetic beads. a) $Q_v = 0.0050$ mL/min. b) $Q_v = 0.0075$

mL/min. c) $Q_v = 0.0100$ mL/min. d) $Q_v = 0.0250$ mL/min.
e) $Q_v = 0.0500$ mL/min. 86

Figure 4.7. Magnetic flux density (B_m) produced by the permanent
magnet. 87

Figure 4.8. Numerical particle tracking at different time at
 $Q_v = 0.0500$ mL/min. a) $t = 0.5$ s. b) $t = 1.0$ s. c) $t = 2.5$ s.
d) $t = 5.0$ s. 88

Figure 4.9. Comparison between experimental and numerical
deposited particles (SPHERO™) on the wall of microchannel. 89

List of Symbols

B_m	Magnetic flux density (T)
C	Concentration (mol/m^3)
D	Mass diffusivity (m^2/s)
d	Thickness (m)
D_e	Electric displacement or electric flux density (C/m^2)
D_m	Microchannel's depth (m)
d_p	Particle diameter (m)
Da	Large-scale Damkhöler number, $Da = K\delta C_{A0}/u_\tau$
Da_s	Small-scale Damkhöler number, $Da_s = Da/f_c$
E	Electric field intensity (V/m)
F	Force (N)
f	Frequency (u_τ/δ)
f_c	Cutting frequency (u_τ/δ)
F_D	Drag force (N)
F_g	Gravity force (N)
F_I	Interaction force (N)
F_M	Magnetic force (N)
F_V	Volume force vector (N/m^3)
g	Gravity ($g = 9.81 \text{ m/s}^2$)
H	Height of the cylindrical cavity (m)
H_m	Magnetic field intensity (A/m)
H_s	Line source half width
I	Intensity (grayscale)
J	Current density (A/m^2)
J_e	Externally generated current density (A/m^2)

K	Kinetic constant of the reaction ($\text{m}^3/\text{mol}\cdot\text{s}$)
L	Microchannel's length (m)
M	Magnetization vector (A/m)
m	Particle mass (kg)
N	Number of events
N_{beads}	Number of beads
P	Pressure (Pa)
p	Pressure
P_D	Number of particles deposited on microchannel walls
P_T	Number of particles introduced in the microchannel
Q_v	Volumetric flow rate (mL/min)
R	Radius of cylindrical cavity (m)
r_i	Position vector of the i^{th} particle (m)
r_j	Position vector of the j^{th} particle (m)
r_p	Radius of particle (m)
Re	Reynolds number based on cylindrical cavity, $Re = \omega R^2/\nu$
Re_b	Reynolds number based on u_b and 2δ , $Re_b = u_b 2\delta/\nu$
Re_τ	Reynolds number based on u_τ and δ , $Re_\tau = u_\tau \delta/\nu$
Sc	Schmidt number, $Sc = \nu/D$
T	Non-reactive scalar
t	Time (s)
u	Streamwise velocity component (m/s)
u_b	Bulk velocity (m/s)
u_p	Velocity of particle (m/s)
u_τ	Friction velocity (m/s)
V	Volume
v	Spanwise velocity component (m/s)
v_e	Velocity of the conductor (m/s)

V_m	Magnetic scalar potential (A)
W	Microchannel's width (m)
w	Wall-normal velocity component (m/s)
x, y, z	Cartesian coordinates (m)
x	Molar fraction
<i>Greek letters</i>	
α	Chemical species
Δ	Increment
δ	Channel half width (m)
$\delta_{\alpha,3}$	Kronecker's delta
ε	Interaction strength (J)
η_D	Refractive index
ϕ	Scalar
λ_2	Second largest eigenvalue of the velocity gradient tensor
μ	Fluid dynamic viscosity (Pa·s)
$\mu_{r,f}$	Fluid relative permeability
$\mu_{r,p}$	Particle relative permeability
μ_0	Permeability of the free space (N/A ²)
ν	Kinematic viscosity (m ² /s)
ρ	Fluid density (kg/m ³)
ρ_e	Electric charge density (C/m ³)
ρ_p	Particle density (kg/m ³)
σ	Standard deviation
σ_c	Collision diameter (m)
σ_e	Electrical conductivity (S/m)
σ^2	Variance
ω	Angular velocity (rad/s)

Subscripts

<i>A</i>	Acid solution
<i>B</i>	Base solution
<i>b</i>	Background
<i>C</i>	Product solution
<i>i</i>	Instantaneous
<i>ideal</i>	Ideal
<i>IN</i>	Inlet or feed
max	Maximum
0	Initial

Symbols

–	Average quantity
‘	Fluctuation
*	Nondimensional

Chapter 0

0. Objectives

The main objective of this thesis is to analyse, experimentally and numerically, chemical reactions at different flow regimes. This thesis is divided to three big blocks: analysis of a chemical reaction in turbulent flows, study of a chemical reaction in laminar and confined flows and, finally, particle deposition on the walls of a microchannel for enzymatic reactions. To accomplish the main objective following tasks have been carried out.

- Numerical analysis of a chemical reaction in a plane turbulent channel flow (Chapter 2).
 - Analyse a database obtained from a direct numerical simulation of the reacting flow in a plane channel.
 - Establish the contribution of the large and small-scale fluctuations in the reacting mass transfers mixing layers.
 - Study the flow structures responsible for the large and small-scale fluctuations of concentration in the mixing layers.
- Numerical and experimental study of a chemical reaction in a confined laminar flow (Chapter 3).
 - Design of the experimental setup to study, simultaneously, the velocity and concentration fields

of the flow using Particle Image Velocimetry (PIV) and Planar Laser Induced Fluorescence (PLIF) techniques.

- Apply PIV to estimate the experimental velocity fields and compare with previous studies.
 - Implement simultaneously the PIV and PLIF techniques to obtain the velocity and concentration fields at the same time.
 - Use Ansys-Fluent software to simulate the confined laminar flow.
 - Compare the numerical and the experimental results for equal working conditions.
- Particle deposition on microchannel walls for enzymatic reactions (Chapter 4).
 - Build a microchannel to analyse the magnetic beads deposition.
 - Analyse the deposition of magnetic beads on microchannel walls.
 - Use COMSOL Multiphysics to simulate the flow in the microchannel.
 - Compare the experimental and numerical results.

Chapter 1

1. Introduction

Scalar transport in turbulent flows plays a fundamental role in a large number of industrial/engineering/environmental applications including chemical reactors, mixing and separation processes and dispersion of pollutants in the atmosphere. Some of these applications may include chemical reactions between different reactants. Mixing is a process in which a non-uniform system becomes uniform. The overall degree of mixing can be separated into two contributions, the large-scale mixing (macromixing) and the small-scale mixing (micromixing). Macromixing is the large-scale mixing -with a naked eye- of fluid elements. On the other hand, micromixing is the molecular-scale mixing of elements of fluid [1][2].

Turbulent mixing has the ability to transport and mix chemical species, energy, and momentum faster than molecular diffusion and, consequently, it is widely used in industrial chemical processes. For a suitable design and optimization of chemical reactors a detailed knowledge of turbulent mixing is needed. For this reason, turbulent mixing has been widely studied, both experimentally and computationally, in the last years [3][4].

One of the main objectives in analysing turbulent mixing is to construct computational fluid dynamic (CFD) models for turbulent

reacting flows. CFD is a helpful tool in chemical reactor design and analysis due to its potential for rapidly generating flow field predictions in different geometries at a relatively low-cost [5][6].

The initial models only considered the time-averaged concentration, temperature and density information, but the influence of the fluctuation intensities on the reaction rate was neglected [7]. Segregation intensity models and, lately, the probability models were developed [5][8]. Originally, the verification of the models for reaction rates was made for gaseous combustion reactions in turbulent flows. Nevertheless, there are differences between mixing of reactants in a gas and a liquid phase. When modelling reacting flows these differences must be considered. The coefficient of molecular diffusion is much larger in gases than in liquids, so the Schmidt number (Sc) in the gas phase is smaller ($Sc \sim 1$) than in liquid phase ($Sc \gg 1$) typically about $Sc = 1000$. Another difference is the density variation of the gas phase, so gas phase density is more sensitive to pressure and temperature variations [3][9]. Baldyga and Bourne [3] considered the specific features of turbulent mixing for flows at $Sc \gg 1$ in Multi-Time-Scale (MTS) model. However, reaction rates models in liquid flows are basically used for $Sc \sim 1$ with specific constants, e.g., modifications of Eddy-Dissipation-Concept (EDC) model [3][9].

Pohorecki and Baldyga [10] carried out experiments in a tubular reactor and confirmed the existence of two different mixing zones in the reactor: the zone of complete segregation and the dissipation zone. Hannon *et al.* [11] used the experimental results from

Pohorecki and Baldyga [10] to check two different chemical reactions models; the Finite-Rate Combustion model, which it was not able to predict the reaction-zone length, and a Presumed-Density-Function (PDF) Multi-Scale-Mixing model. The latter could predict the reaction-zone length using the beta-PDF (instantaneous concentrations).

Fabregat *et al.* [12] performed and analysed direct numerical simulations of a second-order chemical reaction with a Damkhöler number and Schmidt number, $Da = 1$ and $Sc = 0.7$, in an incompressible fully developed turbulent plane channel flow at a low Reynolds number ($Re_\tau = 180$). An additional non-reactive scalar (T) was added in the numerical simulation in order to use it as marker of the non-reactive mixing. The reactive plume was formed when a reactant A was released through a line source into the channel flow doped with reactant B .

In Chapter 2 we analyse the degree of macro- and micromixing of turbulent flow and the large and the small structures responsible for the fluctuations of the different scalars when a second-order chemical reaction takes place. A database of DNS [12] of reactive flow in a plane channel is used for this study.

In order to analyse chemical reactions experimentally, the Particle Image Velocimetry (PIV) and Planar Laser Induced Fluorescence (PLIF) techniques are used. The PIV technique quantifies the velocity fields of the flow and the PLIF technique estimates the degree of mixing or concentration fields of reactive and non-

reactive flows [1][13]. As it is mentioned before, the great majority of authors perform their experimental and computational studies in turbulent regime [1][14].

Fukushima *et al.* [15] investigated the mixing of a passive scalar contaminant with a surrounding fluid in a turbulent free jet. The aim of this study was to obtain a reference data set for investigations of chemically reacting turbulent jets. The main interest was the validation of radial and axial turbulent fluxes of the passive scalar. For this reason, the measurements were carried out using a combined PIV and LIF (Laser Induced Fluorescence) techniques. The validation of the results was made by comparing the measurements with direct numerical simulations, with velocity measurements and with the results of measurements with combined PIV/LIF, PTV (Particle Tracking Velocimetry)/LIF and LDV (Laser Doppler Velocimetry)/LIF. It was found that the velocity fields have good agreement with previous results. However, it was observed some scatter in the axial turbulent flux and an axisymmetric profile in the concentration fluctuation.

Hjertager *et al.* [1] investigated, experimentally and numerically, a fast chemical reaction in a turbulent liquid flow in a channel. The experimental techniques used were PIV and PLIF. The aim of this work was to provide experimental data for validation and to validate CFD models for fast chemical reactions in turbulent liquid flows. The turbulent flow was modelled by solving the 2D Reynolds-Averaged Navier-Stokes equations in combination with the standard $k-\epsilon$ turbulence model. Hjertager *et al.* tested three different reaction

models: the standard eddy dissipation model (EDC), the eddy dissipation concept modified by the multiple time scale turbulent mixer model (EDC-MTS) and the multi-peak PDF model using 5 peaks. They found that the EDC model developed for combustion reactions was inadequate for chemical reactions in liquids. The EDC-MTS model gave a substantial improvement. Overall, the multi-peak PDF model was the better option. However, they reported significant differences in the maximum product concentration and in the minimum product concentration in different zones of the channel length.

Previous studies [1][15] have shown that the analyses of concentration fields in turbulent mixing by means of experimental PIV and PLIF techniques and numerical simulations are not straightforward and in some cases the comparison of results obtained with both approaches are not in good agreement.

One of the objectives of this study is the development of an experimental technique to simultaneously measure the velocity and concentration distributions in liquid reacting flow systems. For this purpose, and as first step, a laminar steady flow configuration has been selected. The application of this approach to turbulent flow is left for future investigation.

Confined flows have a great interest both in basic research and on diverse technological applications. From the industrial point of view, for example, the formation of different flow structures within the fluid can promote or avoid the mixing process. In these sense

cylindrical lid-driven cavities have been extensively studied, numerically and experimentally, in the last 30 years [16][17][18][19][20][21][22][23][24]. The laminar flow behaviour has been analysed in [16][21] and the velocity fields and the formation of vortices have been studied even using the PIV technique [25]. Although the flow field in the laminar regime has been characterized some aspects of the structure of the vortex breakdown, which appears under certain flow conditions, have produced some controversy in the literature.

The first comprehensive experimental study of the cylindrical lid-driven cavity was carried out by Escudier [16] who analysed the flow in a vertical plane and obtained the phase diagram of the visualized flow pattern depending on the Reynolds number and the aspect ratio of the cylindrical cavity. Lopez *et al.* [17] performed simulations in agreement with the visualizations reported by Escudier [16].

Spohn *et al.* [21] carried out experiments and their flow visualizations showed asymmetric vortex breakdown structures at all Reynolds numbers although the cylindrical cavity was nearly perfectly axisymmetric. Previous studies [26] indicated that the origin of the observed asymmetry of the flow can be attributed to the visualization techniques used to highlight the flow structure of the vortex breakdown. Spohn *et al.* [21] demonstrated, using fluorescent dye and the electrolytic precipitation method, that the asymmetry of the flow was not caused by the visualization techniques. They showed that their results were in agreement with

to those reported by Escudier [16], but showed details of the flow structure which were not captured with other visualization techniques. Numerical studies reported in [17][18][19] showed an excellent agreement with the experimental visualizations of [16]. However, details of the vortex breakdown as observed by Spohn *et al.* [21] were not correctly predicted by these simulations. According to Spohn *et al.* [21] the assumption of a perfectly axisymmetric steady flow, as considered in the simulations, implies a closed vortex breakdown structure without fluid exchange between the outer secondary flow and the vortex breakdown. In contrast, their experimental visualizations revealed an open vortex breakdown structure with flow exchange with the outer secondary flow.

Sotiropoulos *et al.* [22] reproduced numerically the asymmetries of the flow observed by Spohn *et al.* [21]. The numerical simulations were carried out in transient mode even the low Reynolds number considered. The Lagrangian tracking of fluid particles near the vortex breakdown revealed that asymmetries are notable at the very early stages of the vortex breakdown formation with an uneven distribution of the fluid particles along the vortex breakdown flow structure.

Brøns *et al.* [23] performed 3D numerical simulations of the flow with two independent perturbations, an inclination of the horizontal fixed wall of the cylinder and an axial displacement in the rotating wall. They showed that a very small displacement of the axis of rotation can reproduce the asymmetries of the flow observed by

Spohn *et al.* [21] and indicated that the origin of the asymmetric flow visualizations can be attributed to small imperfections of the experimental setup.

Chapter 3 considers the experimental and numerical analysis of a laminar, confined and reactive flow in a cylindrical lid-driven cavity with a rotating endwall. The lack of information about confined, reactive and laminar flows makes this study interesting, taking into account that even the flow is laminar the system exhibits vortex breakdown phenomena [16]. It should be noted that even the laminar flow can be less attractive from the industrial point of view it allows a simpler comparison between the experimental and computational results than in turbulent flows and, furthermore, allows the validation of the experimental techniques. The steady laminar flow in a cylindrical lid-driven cavity enables us to focus in the analysis of the chemical reaction and in the simultaneous applications of the PIV and PLIF techniques.

As a first step to analyse enzymatic reactions in microchannels [27][28], the last part of this thesis considers the deposition rates of magnetic beads on the walls of a microchannel produced by the effect of a permanent magnet.

In the last years, magnetic micro-beads are widely used for medical diagnostics, pharmaceutical research and biological research. Specifically, these studies deal with the isolation of specific cells for immunomagnetic assays, separations of proteins, targeted drug delivery and application of mechanical forces to cells [29].

Magnetic micro-beads can be easily immobilized to using permanent magnets. This is why they are an attractive alternative to traditional monolithic microfluidics that needs complex structure for wall reactions. Magnetic particles can be washed away from the channel unlike monoliths which are more or less permanent. Furthermore, the magnetic forces exerted on magnetic beads can improve their mixing, focus particles for immunoagglutination assays, and serve as a detection mechanism for immunoassays [30].

Wang *et al.* [31] presented a technique to capture and separate biomolecules using magnetic bead movement on a chip. The microchip consisted of two well reservoirs connected via microchannel. Different magnet velocities were tested to move the magnetic beads between the two wells. The magnetic beads used were spherical superparamagnetic streptavidin coated Dynabeads® M-280. Enzymatic reactions were employed to test the microchip.

The particles can have different magnetic properties, such as ferromagnetism, paramagnetism and superparamagnetism. Ferromagnetic materials are those which become magnetized in a magnetic field and retain their magnetic properties when the magnetic field is removed. On the other hand, in paramagnetic materials once the magnetic field is removed their magnetism disappears [32]. Superparamagnetic materials have a type of magnetism that occurs in small ferromagnetic particles. Superparamagnetic particles have a short relaxation time, that is, the time in which magnetization goes to zero after the effect of an

external magnetic field. Therefore, their magnetic moments are quickly reoriented [33].

In Chapter 4, the magnetic micro-beads deposition rate on the walls of microchannel is analysed. The micro-beads deposition is induced by a permanent magnet. Two different types of magnetic micro-beads are tested: SPHERO™ Carboxyl Magnetic and Dynabeads® M-270 Carboxylic Acid. The SPHERO™ beads are paramagnetic beads and are prepared by coating a layer of magnetite and polystyrene onto monodispersed polystyrene core particles [32]. Dynabeads® particles are uniform, monosized superparamagnetic beads coated with a hydrophilic layer of glycidyl ether, followed by further coating with carboxylic acid groups [34]. It is reported the morphology of the micro-beads cluster that deposit on the microchannel wall at different flow rates. This study addresses experimental and numerical aspects of the micro-beads deposition. Additionally our results open the prospect for further analysis such as the enzymes immobilization on the magnetic beads surface and the corresponding kinetic enzyme reaction study in the microchannel [35].

Chapter 2

2. Chemical Reaction in a Plane Turbulent Channel Flow

Fabregat *et al.* [12] performed and studied direct numerical simulations of a second-order chemical reaction with a Damkhöler number and Schmidt number, $Da = 1$ and $Sc = 0.7$, in an incompressible fully developed turbulent plane channel flow at a low Reynolds number ($Re_\tau = 180$). An additional non-reactive scalar (T) was added in the numerical simulation in order to use it as marker of the non-reactive mixing. The reactive plume was formed when a reactant A was released through a line source into the channel flow doped with reactant B .

The objective of this chapter is to analyse the degree of macro- and micromixing of turbulent flow and the large and the small structures responsible for the fluctuations of the different scalars analysed when a second-order chemical reaction takes place. A database of a DNS of the reactive flow in a plane channel [12] is used to perform this study.

2.1. Physical and Mathematical Model

The channel configuration consists in two parallel, infinite and smooth walls separated a distance $L_z = 2\delta$, where δ is the channel

half width. The fluid flows between these walls driven by a constant mean pressure gradient along the streamwise direction. Figure 2.1 shows a schematic representation of the computational domain.

The coordinate system origin is located at point O . The streamwise (x) and spanwise (y) directions are considered homogeneous in terms of momentum transport. The spanwise direction is also considered homogeneous for the mass transport. The concentrations of the chemical species are imposed at the channel inlet and advective boundary conditions are used at the outlet. The reactant A is released through a source line with size $2H_s = 0.4\delta$. The source is located at the inlet of the channel and it is centered between the walls (see Figure 2.1).

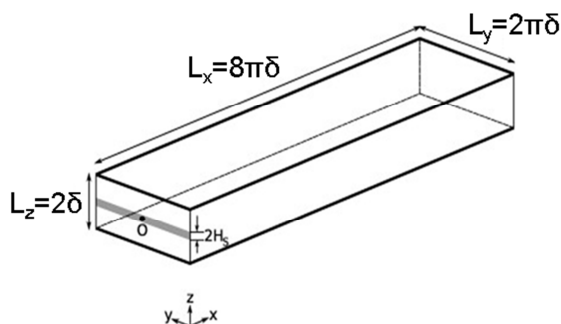


Figure 2.1. Schematic representation of the computational domain with dimensions $L_x \times L_y \times L_z = 8\pi\delta \times 2\pi\delta \times 2\delta$. The domain is discretized using a staggered grid with a resolution of $258 \times 130 \times 130$ control volumes.

The reactant B is opened up near the walls of the channel. It is analysed the segregated case considered by Fabregat *et al.* [12], in which reactant B is not found in the feed of A and reactant A is not found where B enters the channel. The second-order chemical

reaction between the two reactants (A and B) to form a product (C) is indicated below.



The flow is assumed to be incompressible, isothermal and the fluid properties, constant. The continuity equation for an incompressible flow is:

$$\frac{\partial u_i^*}{\partial x_i^*} = 0 \quad (2.2)$$

where $u_i^* = u^*, v^*, w^*$ are the velocity components along the streamwise (x), spanwise (y) and wall-normal direction (z), respectively. Using δ , u_τ and C_{A0} as space, velocity and mass concentration scales, respectively, the non-dimensional momentum and mass transport equations are:

$$\frac{\partial u_i^*}{\partial t^*} + \frac{\partial u_i^* u_j^*}{\partial x_j^*} = 1 - \frac{\partial p}{\partial x_i^*} + \frac{1}{\text{Re}_\tau} \frac{\partial^2 u_i^*}{\partial x_j^* \partial x_j^*} \quad (2.3)$$

$$\frac{\partial C_\alpha^*}{\partial t^*} + \frac{\partial C_\alpha^* u_j^*}{\partial x_j^*} = \frac{1}{\text{Re}_\tau \text{Sc}} \frac{\partial^2 C_\alpha^*}{\partial x_j^* \partial x_j^*} + (2\delta_{\alpha,3} - 1) \text{Da} C_A^* C_B^* \quad (2.4)$$

where $\delta_{\alpha,3}$ is the Kronecker's delta with $\alpha = 1, 2, 3$ for the chemical species A , B and C , respectively. The first term on the right-hand side of Equation 2.3 is the non-dimensional averaged pressure gradient imposed along the streamwise direction. The non-dimensional parameters in Equations 2.3 and 2.4 are the Reynolds

number, the Schmidt number and the Damköhler number for a second-order chemical reaction. The Reynolds number, Re_τ , is set to 180 ($Re_b = 5452$) and Sc and Da are set to 0.7 and 1, respectively. It is assumed that the coefficients of molecular diffusion are identical for A , B and C , so $D_A = D_B = D_C = D$.

The transport equation (Equation 2.5) of a conserved scalar (T) has been also solved simultaneously to the momentum and mass transport equations (Equations 2.2-2.4) to determine the effect of the turbulent mixing in the chemical reaction.

$$\frac{\partial T}{\partial t^*} + \frac{\partial T u_j^*}{\partial x_j^*} = \frac{1}{Re_\tau Sc} \frac{\partial^2 T}{\partial x_j^* \partial x_j^*} \quad (2.5)$$

The boundary conditions for the conserved scalar T are the same as those of the reacting specie A . Equations 2.2-2.5 constitute the mathematical model of the DNS of incompressible flows with constant physical properties. Alternative approaches to simulate reactive flows are the numerical resolution of the modelled time-averaged transport equations [3][5] and the methods based on the solution of the modelled transport equations for the velocity-composition joint PDF [36].

The reaction is assumed to occur under isothermal conditions. The concentration of the reactant A at the source is $C_{A0}^* = C_A^*(0, y^*, \pm H_s, t^*) = 1 \quad \forall z \in [-H_s, H_s]$ and $C_A^*(0, y^*, z^*, t^*) = 0 \quad \forall z \notin [-H_s, H_s]$. The concentration at the inlet for reactant B is

$C_{B0}^* = C_B^*(0, y^*, \pm H_s, t^*) = 0.05 \quad \forall z \notin [-H_s, H_s]$ and
 $C_B^*(0, y^*, z^*, t^*) = 0 \quad \forall z \in [-H_s, H_s]$. The concentration of the product C at the inlet is zero $C_{C0}^* = C_C^*(0, y^*, z^*, t^*) = 0$. The concentration of the non-reactive scalar, T , at the source is the same of reactant A . The concentration fields have been initialized as $C_A^* = 0$, $C_B^* = 0.05$, $C_C^* = 0$ and $T = 0$. The database analysed in the present study contains the time-evolution of the velocities and scalars in each grid node of the computational domain when the flow and the concentration distributions were statistically in steady state. The record has 4200 time steps ($\Delta t = 5 \cdot 10^{-3} \delta/u_\tau$) that correspond to a total time of 21 δ/u_τ . More details about the boundary conditions and control volumes can be found in Sancho *et al.* [14].

2.2. Mixing Contribution

The time evolution of the fluctuations of the concentration of the species at each grid node have been used to evaluate the degree of macro- and micromixing. As an example, Figure 2.2 shows the time evolution of the fluctuations of concentration of the reactive scalar A for $t \leq 5 \delta/u_\tau$ at the position $x^* = 4.8$, $y^* = 0$ and $z^* = 0.25$. The large frequency component of the signal corresponds to the small-scale fluctuations of the flow (Figure 2.2c) and, consequently, it can be assumed that these fluctuations are linked with the micromixing. On the other hand, the small frequency components of the fluctuations can be associated with the large-scale structures

of the flow and they can be related to the macromixing (Figure 2.2b).

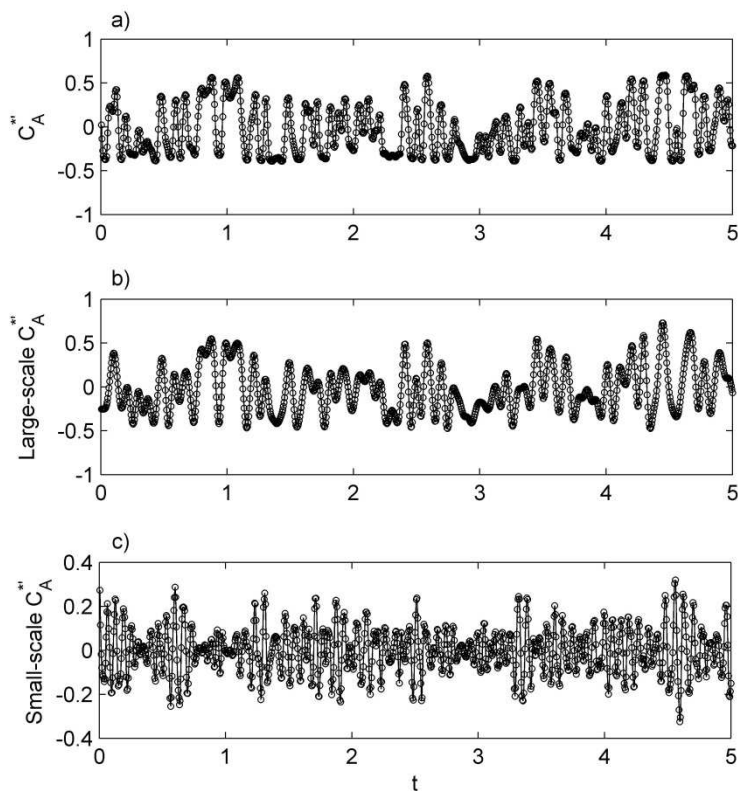


Figure 2.2. Time-evolution of a) fluctuations of the dimensionless concentration of A , b) large-scale fluctuations of the dimensionless concentration of A and c) small-scale fluctuations of the dimensionless concentration of A at $x^* = 4.8$, $y^* = 0$ and $z^* = 0.25$.

The small and the large-scale contributions can be separated to determine the role of the macro- and micromixing in the chemical reaction. The separation of the scales has been carried out in the frequency domain using a wavelet filter. As an example, Figure 2.3 shows the spectrum computed with the complete time evolution

($0 \leq t \leq 21\delta/u_\tau$) of the signal shown in Figure 2.2a corresponding to the fluctuations of A at $x^* = 4.8$, $y^* = 0$ and $z^* = 0.25$. The cutting frequency of the filter has been set within the inertial subrange ($f \approx 15 u_\tau/\delta$) and the resulting large-scale and small-scale spectra are shown in Figure 2.3. The wavelet decomposition used satisfies that the sum of the two spectra and of the two decomposed signals equals the original spectrum and the original signal, respectively.

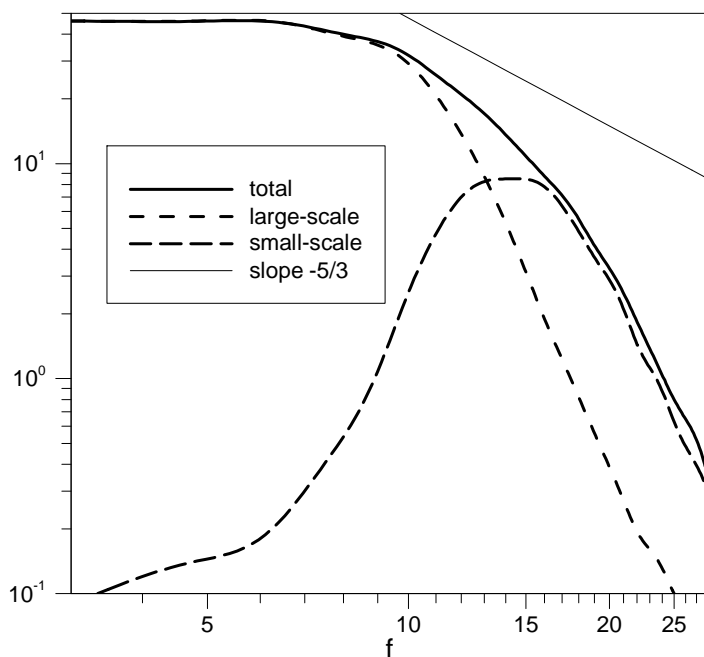


Figure 2.3. Spectra of signals shown in Figure 2.2. The cutting frequency used for the separation is $f \approx 15 u_\tau/\delta$.

The division of the spectra into two regions allows the calculation of the time evolution of the large-scale fluctuations and the time

evolution of the small-scale fluctuations for the scalars. Figures 2.2b and 2.2c show, respectively, the large-scale contribution and the small-scale contribution for the signal shown in Figure 2.2a. To quantify the contribution of each scale to the mixing for the different variables (ϕ), their variance has been computed (Equation 2.6). Figure 2.4 shows the total variance and the variances of the small and large-scale fluctuations of C_A^* scaled with $\sigma^2 / \left[\overline{C_A^*} (1 - \overline{C_A^*}) \right]$, which has a value between 0 and 1; notice that $\sigma^2 / \left[\overline{C_A^*} (1 - \overline{C_A^*}) \right]$ represents the largest possible value of the variance for given $\overline{C_A^*}$. Figure 2.4a corresponds to the centerline ($z^* = 0$) of the channel and Figure 2.4b to the position $z^* = 0.25$, which is near the concentration mixing layer located at $z^* = 0.20$. The variances have been averaged along the spanwise direction.

$$\sigma^2 = \frac{1}{N} \sum_{i=1}^N (\phi_i - \overline{\phi})^2 \quad (2.6)$$

As expected, at the center of the channel, $z^* = 0$, (Figure 2.4a), the variance is lower than at the mixing layer, $z^* = 0.25$, (Figure 2.4b). It can be observed in both plots that the total variance is similar to the variance of the large-scale fluctuations, being almost equal at the end of the channel, indicating that only the large-scale flow fluctuations produce fluctuations of the concentration of A .

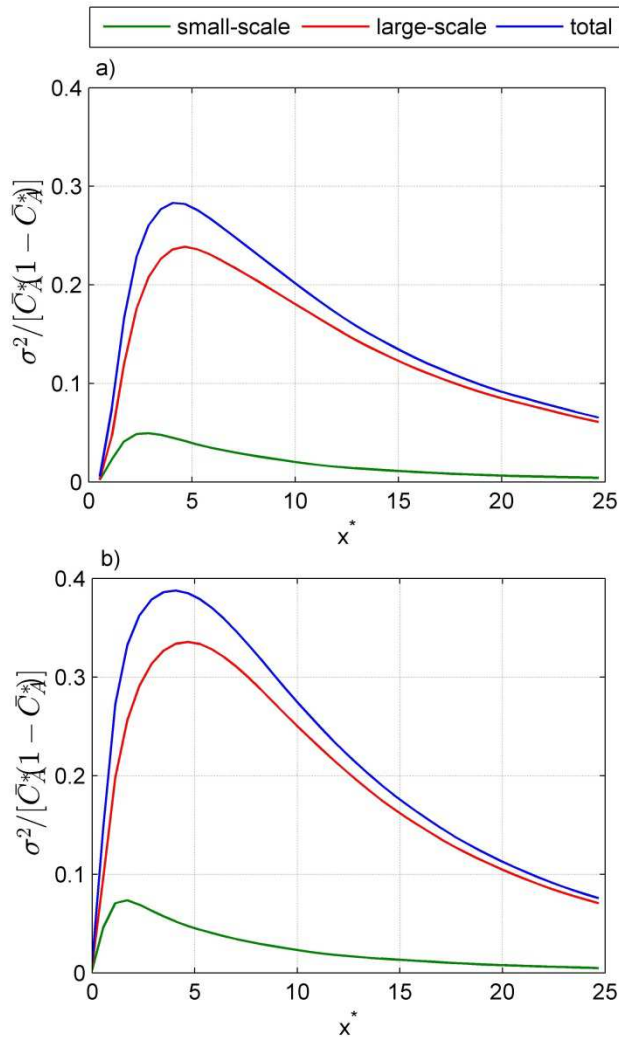


Figure 2.4. Variance of concentration of A normalized with $\sigma^2 / [\overline{C_A^*}(1 - \overline{C_A^*})]$.

a) At the centerline of the channel ($z^* = 0$) and b) near the interface of the concentration mixing layer ($z^* = 0.25$).

The small-scale and the large-scale mixing contributions, defined in Equations 2.7 and 2.8, of the reactive scalars A , B and C at the centreline ($z^* = 0$) are shown in Figure 2.5.

$$\text{Mixing contribution of small-scale} = \frac{\sigma_{\text{small-scale}}^2}{\sigma_{\text{total}}^2} \quad (2.7)$$

$$\text{Mixing contribution of large-scale} = \frac{\sigma_{\text{large-scale}}^2}{\sigma_{\text{total}}^2} \quad (2.8)$$

It can be seen that the small and the large-scale at the inlet of the channel contribute equally to the total variance. Along the streamwise direction the large-scale contribution increases and near the outlet the contributions of the large-scale and small-scale fluctuations of the concentrations are about 90% and 10% respectively. The mixing contribution of velocities can be seen in Sancho *et al.* [14].

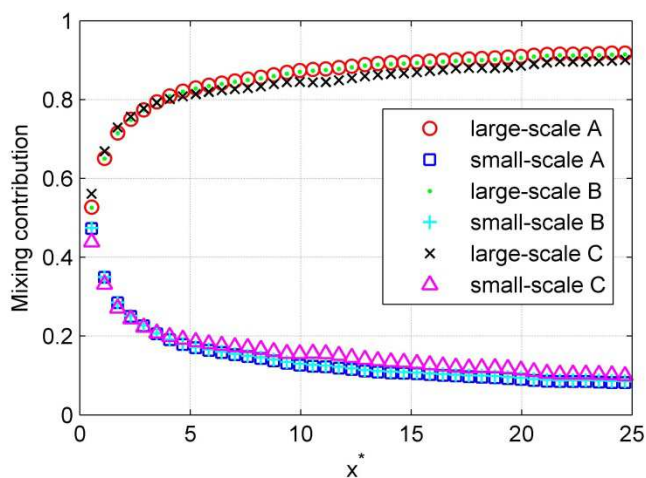


Figure 2.5. Mixing contribution of reactive scalars at the centerline ($z^* = 0$).

Figure 2.6a shows the comparison of the time averaged profiles of the reactive (A) and the conserved (T) scalar at $z^* = 0$. Note that the reactive scalar A and the non-reactive scalar T have the same

inlet conditions and the only difference between them is their behaviour in the chemical reaction.

It can be seen that the small difference found at the outlet corresponds to the small conversion of A (5%) obtained for the conditions considered.

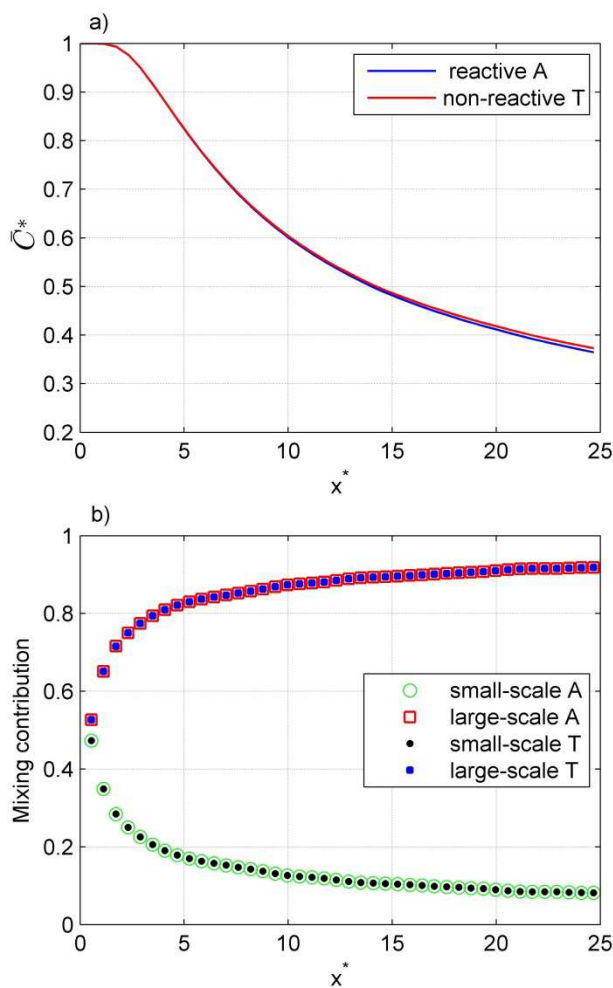


Figure 2.6. a) Time-averaged concentration at the centerline ($z^* = 0$) of reactive scalar A and non-reactive scalar (T). b) Mixing contribution of A and T .

The mixing contribution for A and T (Figure 2.6b) are almost coincident for the two variables indicating that the chemical reaction has not an important effect in the mixing, which is completely dominated by turbulence. This can be explained also taking into account that the small-scale, defined here using cutting frequency $f_c \approx 15u_\tau/\delta$, has a Damkhöler number $Da_s = Da/f_c$. This means that this reaction is very slow to small-scale and can be used as a test system for large-scale only, as small-scale effects on reaction are negligible.

2.3. Analysis of the Flow Structures

The spatial distributions of the velocity and concentration fields is also analysed on the plane yz at $x^* = 3$ where, on average, the reactants are mainly segregated. The database used contains the time evolution during 4200 time steps of the three components of the velocity vector and the three reactive scalars on this plane. This period of time corresponds to $t = 21 \delta/u_\tau$. It is applied a conditional pattern recognition technique based on the detection of extreme values of the large-scale fluctuations and of the small-scale fluctuations of reactive scalar A to obtain the ensembles average of the flow structures responsible for these fluctuations.

Figure 2.7 shows a sketch of the steps of conditional sampling procedure used for the selection of the events. The first step consists on the computation of the cross-correlation between a template, see Sancho *et al.* [14], and the instantaneous spatial two-dimensional

distributions of the large-scale or of the small-scale fluctuations of A in the plane $x^* = 3$ for all the recorded time steps.

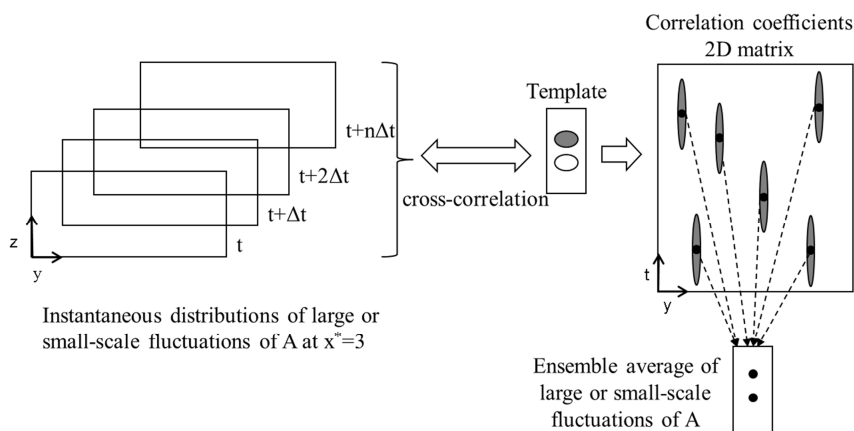


Figure 2.7. Steps of the conditional sampling procedure.

It can be seen in Figure 2.7 that the correlation coefficients, obtained for a given template, are stored in a two-dimensional matrix (i.e., a vector for each time step). The regions where local maxima of correlation occur conform areas that are elongated in time, according to the time history of the values of large-scale fluctuations and small-scale fluctuations of A . In these areas, only the time at which the absolute maximum of correlation occurs is selected as an event for averaging. The use of two sets of templates produced the detection in the database of 714 events corresponding to the large-scale fluctuations and 413 corresponding to the small-scale fluctuations. The large-scale events explain 27% of the time evolution while the small-scale events represent about 11% (i.e. a total of 38%). The mean duration of the events and the computation of number of events can be seen in Sancho *et al.* [14].

When an event occurred, the flow and the concentration fields are sampled in a box with a streamwise extension of $2.50 < x^* < 3.80$ to reduce the flow structures responsible for the large and the small-scale fluctuations of A . The flow topology of large-scale fluctuations of A is depicted in Figure 2.8 in terms of the isosurface of a negative value of the second largest eigenvalue of the velocity gradient tensor (λ_2), a quantity proposed by Jeong *et al.* [37] to detect the occurrence of vortex cores.

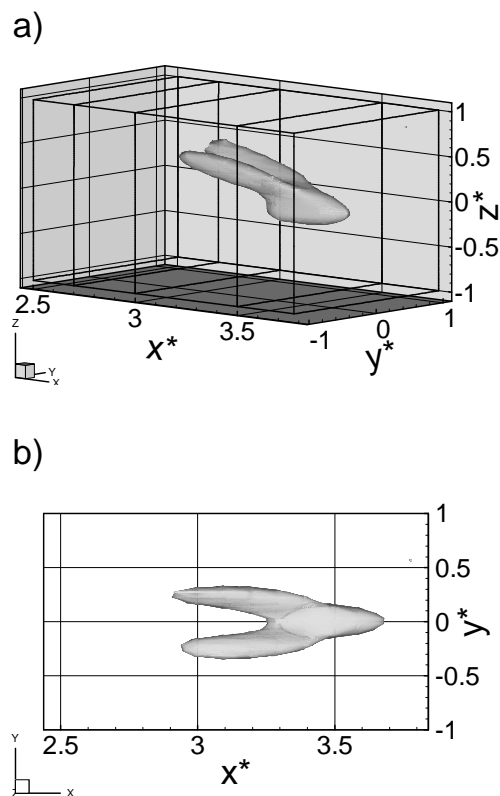


Figure 2.8. Conditionally sampled flow responsible for the large-scale fluctuations of A . Flow topology A in terms of the isosurface $\lambda_2 / \text{Min}(\lambda_2) = -0.39$. a) 3D view and b) top view.

The contours of the fluctuations of A and C are shown in Figure 2.9a and 2.9b together with the in-plane velocity field. Note that the time-averaged streamwise velocity profile has been subtracted from the conditional sampled flow and the streamwise scale of the plots in Figure 2.8 and Figure 2.9 has been enlarged in comparison with the spanwise and normal to the wall scales.

As it can be seen in Figure 2.8 the conditional sampled flow structure responsible for the large fluctuations of A has a hairpin shape. The legs of the hairpin are inclined about 35° in the xz plane (see for example Figure 2.9a) and they cross the top mass transfer mixing layer. The head of the hairpin located at the center of the channel ($z^* \approx 0$) generates, in terms of velocity fluctuations, a large recirculation. In terms of absolute velocities this recirculation corresponds to an acceleration of the flow at the bottom of the head and a deceleration at the top of the head (see Figure 2.9a). The corresponding fluctuations of B , not shown for sake of brevity, follow the inverse trend (i.e. large positive fluctuation of B in the top mixing layer and a large negative fluctuation in the bottom one). The fluctuations of C are shown in Figure 2.9b. It can be seen that the top negative/positive fluctuation of A/B , located at $z^* > 0$, produces a negative and a positive fluctuation of C . At $z^* < 0$ the excess of A produces a negative and a positive fluctuation of C .

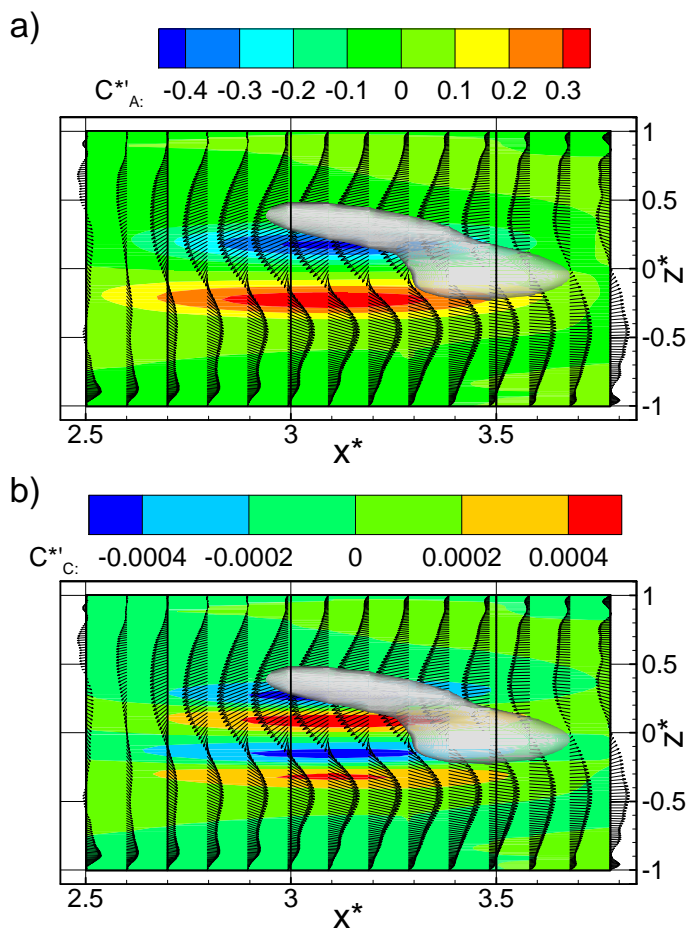


Figure 2.9. Side view of the flow topology shown in Figure 2.8. Contours of the dimensionless large-scale fluctuations of a) reactive scalar A and b) reactive scalar C .

Figure 2.10 shows the conditional sampled flow in the vertical plane $y^* = 0$ in terms of contours of the small-scale fluctuations of A and C and the in-plane velocity vectors. Note that the time averaged streamwise velocity profile has been subtracted from the conditionally sampled flow.

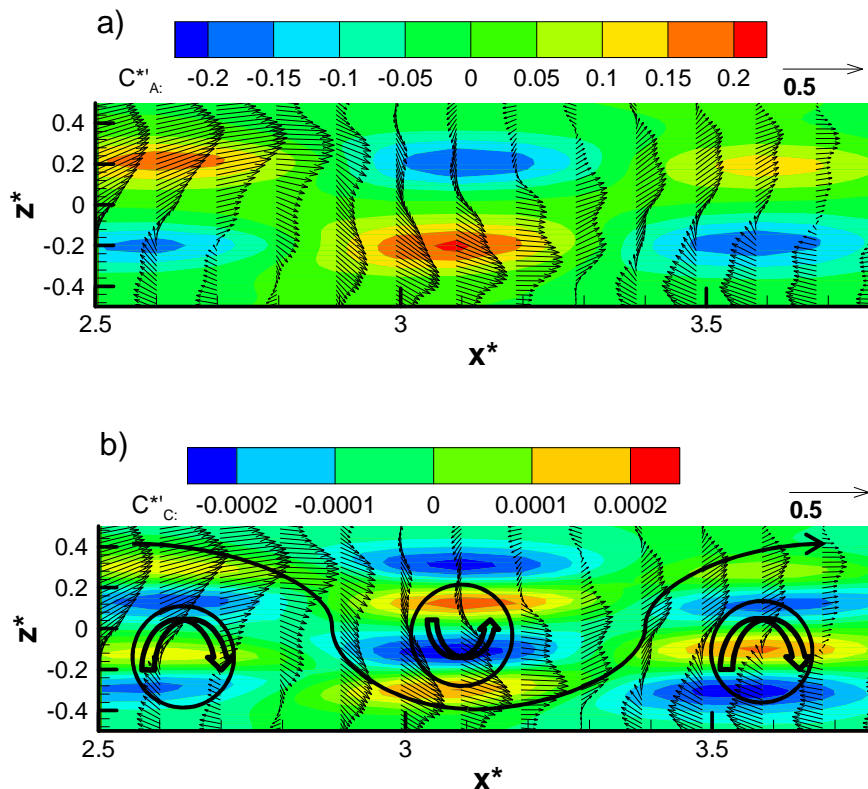


Figure 2.10. Contours of the dimensionless small-scale fluctuations of a) reactive scalar A and b) reactive scalar C .

It can be seen in Figure 2.10a that, in the case of small-scale fluctuations of A , the flow structure consists in a periodic distribution of counter rotating eddies along the streamwise direction that are located in the central part of the channel and convect flow from one mass transfer mixing layer to the other one. The pattern of the contours of concentration of A (Figure 2.10a) consist in a periodic distribution along the streamwise direction of three pair of lobes that alternate sign. Each pair of lobes, composed by a positive and a negative region distributed along the z -direction is produced by a flow structure that convects flow from one mixing

layer to the other one, in a similar way, but with a smaller length scale, than the flow structure shown in Figure 2.9a responsible for the large-scale fluctuations of concentration. The same happens with small-scale fluctuation of C (Figure 2.10b) but instead of being pairs of lobes like Figure 2.10a, there are four lobes, two positives and two negatives regions, that alternate sign. Negative lobes indicate the presence of unreactive A or B .

2.4. Conclusions

In this study a database of a direct numerical simulation of the reactive flow in a plane channel is analysed. One reactant is introduced in the central region of the channel and the other near the walls of the channel. This distribution generates two mass transfer mixing layers distributed symmetrically with respect to the center of the channel. The time evolutions of the fluctuations of concentration have been decomposed into a large-scale and a small-scale contribution, using a wavelet filter. The small and the large-scale fluctuations at the inlet of the channel contribute equally to the total variance. Along the streamwise direction the large-scale contribution increases and near the outlet of the channel the contributions of the large-scale and small-scale fluctuations of the concentrations are about 90% and 10%, respectively. The flow structure responsible for the large-scale fluctuations of concentration in the mixing layers has a hairpin shape. The head of the hairpin produces an intense flow entrainment in the mass transfer mixing layers. The flow structure of responsible for the small-scale fluctuations consist in a periodic distribution along the

streamwise direction of counter rotating eddies that are located in the central part of the channel and convect flow from one mass transfer mixing layer to the other one.

Chapter 3

3. Chemical Reaction in a Confined Laminar Flow

The aim of this chapter is to analyse, experimentally and numerically, an axisymmetric, confined, reactive and laminar flow in a cylindrical cavity with a rotating endwall.

3.1. Experimental Setup

The experimental setup consists of a polymethyl methacrylate (PMMA) cylindrical container with an inner radius of $R = 0.04$ m and with a rotating wall at the top, see Figure 3.1. The rotating wall is driven by an electronically controlled DC motor, operating at angular velocities between $\omega = 5$ and $\omega = 25$ rad/s. These angular velocities correspond to Reynolds number (Equation 3.1) between 1000 and 2300. The aspect ratio of the cavity is set to $H/R = 2$.

$$\text{Re} = \frac{\omega R^2}{\nu} \quad (3.1)$$

where ω is the angular velocity (rad/s), R is the radius (m) and ν is the kinematic viscosity ($\sim 10^{-5}$ m²/s).

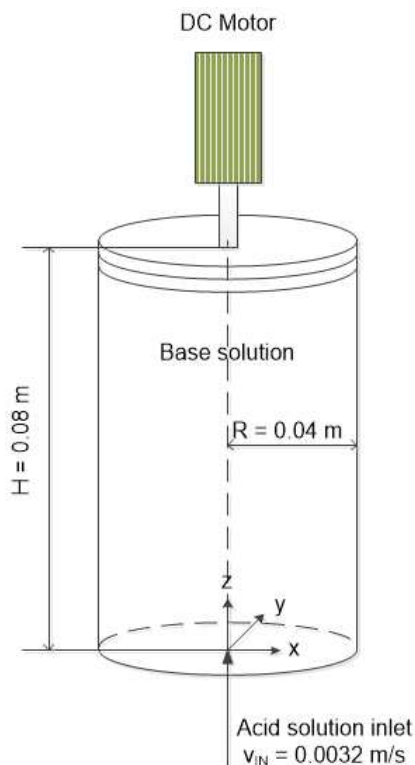
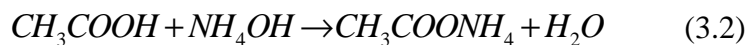


Figure 3.1. Sketch of the experimental setup.

The chemical reaction considered is a fast irreversible neutralization acid-base reaction, i.e.:



The reaction constant (K) is of order $10^8 \text{ m}^3/\text{mol}\cdot\text{s}$ [1] and the concentration of the Acetic Acid (A) and Ammonium Hydroxide (B) are, respectively, 0.1 M and 0.01 M. The base solution (B) is initially inside the cylindrical cavity. The acid solution (A) is introduced in the cavity through the bottom inlet of 3 mm of

diameter with a syringe pump (CHEMYX Fusion 100). The velocity inlet of the acid solution is $v_{IN} = 3.2$ mm/s. This velocity is 50 times smaller than the average velocity of the rotating top wall for $Re = 1000$ and it does not affect significantly the velocity distribution imposed by the rotating wall, see section 3.3.3. The acid solution is introduced to the cylindrical cavity when the flow is in steady state, after 5 minutes, during 30 minutes and the total volume is 40 mL, see section 3.4. The total volume of the base is 400 mL, so at the end of the experiment the base solution would be totally consumed if the reaction would be complete.

The fluid is a water-glycerine (60% v/v glycerine) solution of acid and base with kinematic viscosity $\nu \sim 10^{-5}$ m²/s and density $\rho \sim 1100$ kg/m³. To eliminate shadows and interference effects in the images due to curvature of the cylindrical wall, the container is immersed in a rectangular box filled with an aqueous solution of 60% v/v of glycerine, with the same viscosity and density as the reacting mixture. The solution and PMMA have similar refractive indexes ($\eta_{D, glycerine 60\%} = 1.42$ [38] and $\eta_{D, PMMA} = 1.49$ [39]). Figure 3.2a shows a picture of the cavity inside of the rectangular box and Figure 3.2b shows a picture of the experimental setup.

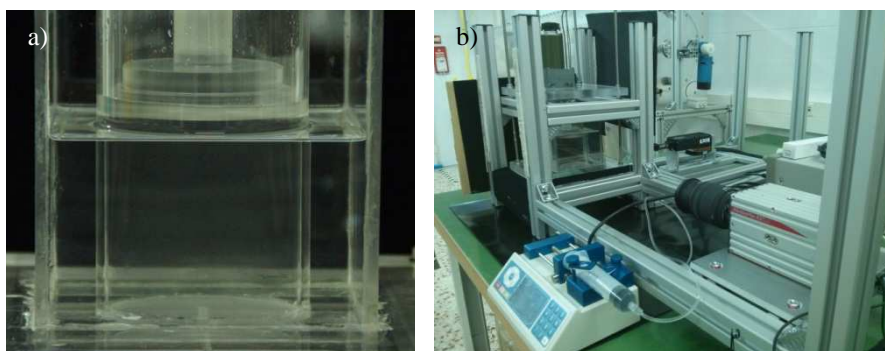


Figure 3.2. a) Picture of cylindrical cavity and rectangular box. b) Picture of the experimental setup.

3.1.1. Light Source and Image Acquisition

To perform the experiments detailed in section 3.1, an illumination system and digital cameras are required.

The illumination system used in this work is a Nd: YAG semiconductor laser (Monocrom MP532-3W), linearly polarized with 532 nm wavelength. In the experiments it has been used in continuous mode at 3 W. The optical system is composed of 2 lenses beamforming and another one to generate the sheet. The light sheet is about 1 mm thick.

The images are recorded using two cameras: MotionPro HS-3 and MotionProX3. Both cameras are equipped with a 1" CMOS sensor with 1280×1024 pixels with size $12 \mu\text{m}$. Each camera is equipped with a zoom Sigma, 28 - 300 mm F 3.5 - 6.3 DG Macro.

3.2. Experimental Techniques

The experimental techniques used are optical techniques widely studied in the last years. In the following sections, a review of Particles Image Velocimetry (PIV) (section 3.2.1) and Planar Laser Induced Fluorescence (PLIF) (section 3.2.2) are explained. In section 3.2.3 the simultaneous application of PIV and PLIF is discussed.

3.2.1. Particle Image Velocimetry Technique

In the last years, different methods to measure the velocity fields of the fluid have been developed using the digital image processing. One of the most used methods is the Particle Image Velocimetry (PIV). This method has the advantage of being no-intrusive, indirect and accurate measuring the velocity fields of the fluid. The method was developed by Adrian in 1984 [40]. In the following years the method was generalized by various authors [41][42][43][44][45].

The basic experimental setup consists in illuminating the fluid region to be studied using a thin laser sheet and capturing, at least, two consecutives images by a digital camera. In order to visualize and measure the velocity fields of the fluid, the tracer particles have to meet the following requirements [43].

- Have a particle density similar to fluid density.
- Be enough small to follow the fluid movement and not interfere in it.

- Be large enough to be able to reflect the light of laser sheet and analyse the fluid movement.

The light scattered by the particles is recorded using a digital camera, thus generate a series of images separated by a time interval (Δt). An important condition for achieving optimal implementation of the method is that the time between two consecutives images has to be short enough so that the tracers particles appearing in an image also appear in the next, and long enough, in order to appreciate the particles movement. In Figure 3.3, it can be seen a schematic arrangement for PIV.

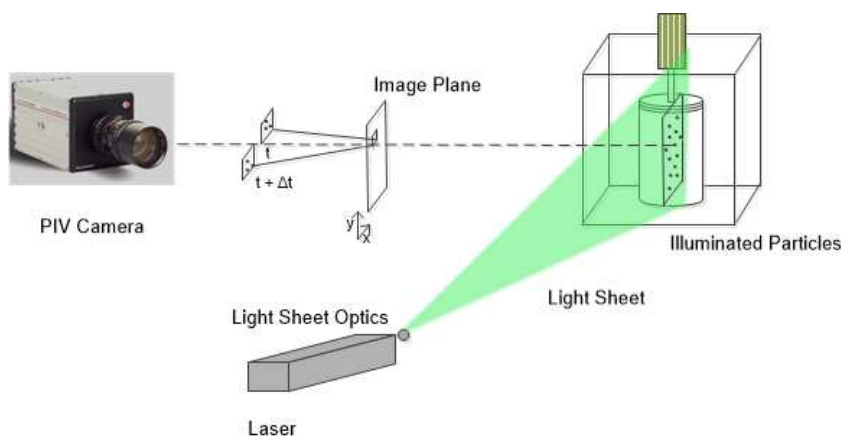


Figure 3.3. Sketch of Particle Image Velocimetry (PIV) arrangement.

The implementation of the standard algorithm of PIV is based in the statistical method, allowing estimate the particles movement using a cross-correlation. For this purpose, every image is divided in subdivisions called interrogation windows. It is assumed that all particles inside the interrogation window have a uniform movement during the period of time between every image. In order to solve flow structures smaller than interrogation window, the Local Field

Correction Particle Image Velocimetry (LFCPIV) is used [46]. This method has a remarkable capability to solve the small-scale structures of the flow. The interrogation window has a typical size between 8 and 128 pixels. Figure 3.4 shows up the conceptual arrangement of PIV technique.

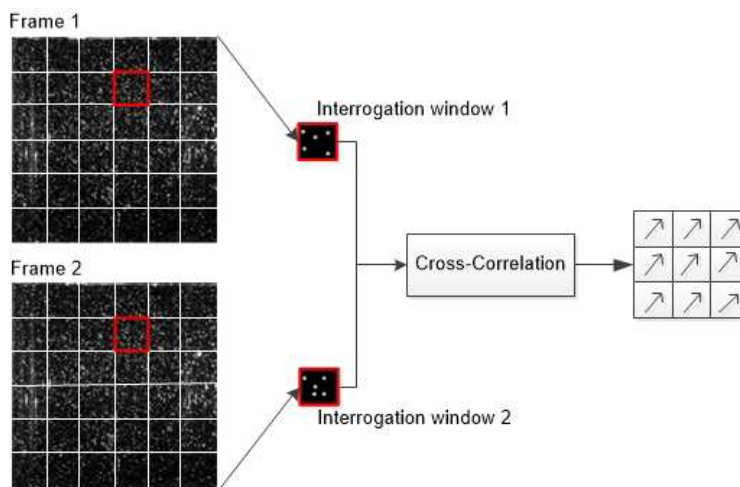


Figure 3.4. Conceptual arrangement of Particle Image Velocimetry (PIV) technique.

In this study, the image processing has been made through a Matlab program set of routines by means of simple algorithms. The program consists of one main Matlab GUI that calls the several external files. This PIV Matlab package has been developed by several members of ECoMMFiT group. The Matlab GUI contains many options which can be changed for the necessary conditions of the flow and the image properties. Some of these options are related with higher methods that improve the performance and accuracy of the PIV technique. The most important options are explained in [44].

Therefore, to obtain the velocity fields of the flow, the PIV technique has been used [42][45][46]. The measurement procedure is based on the cross-correlation of the three consecutive images, improving the peak detection in comparison with the usual cross-correlation of the two consecutive images [47]. The interrogation window has a size of 32×32 pixels with an overlapping of 16 pixels. The particles used are neutrally buoyant alginate particles (see section 3.2.1.1 for details about particles). A vertical green laser sheet of 3 W, with 1 mm of width is used as illumination system, see section 3.1.1. The sheet is focalised in two positions, the vertical and the horizontal plane. The vertical plane is focalized along the x and z -direction at $y^* = 0$ ($y^* = y/R$). The horizontal plane is situated at different axial positions (z^*) along the x and y -direction. The PIV camera is a MotionPro HS-3 (see section 3.1.1) and is placed creating an angle of 90° with the laser sheet, see Figure 3.5. The images are recorded at 100 frames per second corresponding to 800×800 pixels window size. Figure 3.6 shows images captured during PIV experiments.

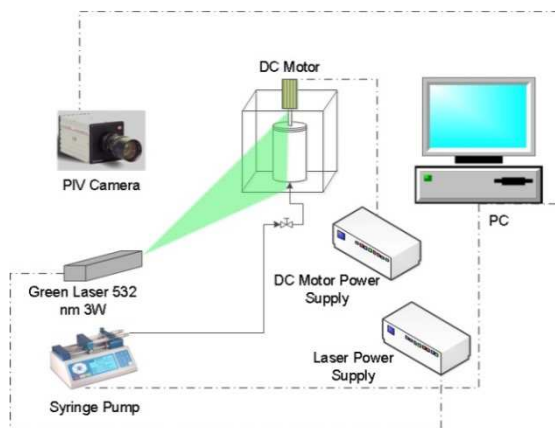


Figure 3.5. Sketch of the experimental setup of PIV experiments.

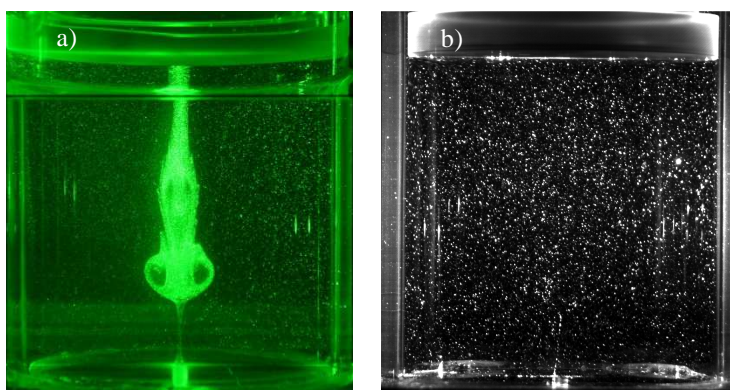


Figure 3.6. Images captured during PIV experiments at $Re = 2000$. a) Colour digital camera and b) PIV camera.

3.2.1.1. Tracer Particles

The particles used for PIV are neutrally buoyant alginate particles of diameter between 50 and 100 μm . The particles have been functionalized with rhodamine [48]. Rhodamine B has the peak absorption (excitation) at wavelength around 555 nm. The emission occurs at the wavelength around 575 nm. Figure 3.7 shows the absorption and emission of rhodamine B [49].

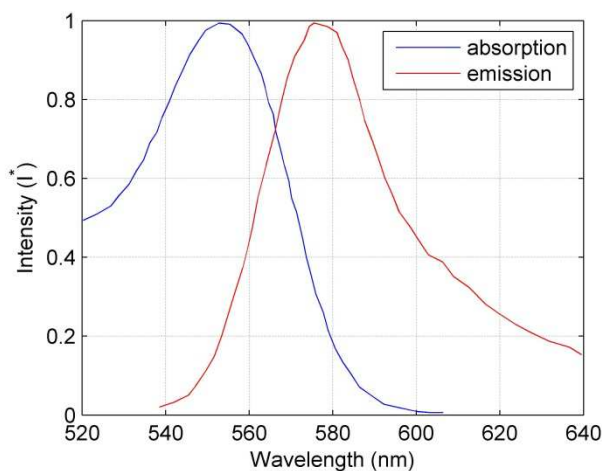


Figure 3.7. Absorption and emission wavelength of rhodamine B.

3.2.2. Planar Laser Induced Fluorescence Technique

Planar Laser Induced Fluorescence (PLIF) is an optical technique that has been extensively used for flow visualization and quantitative measurements such as species concentrations or temperature. A good description of the principles of the technique was made by Walker (1987) [50]. Therefore, a brief description of the technique is made in what follows.

The flow to be studied is stained with a dye (fluorescent tracer). Using a light source (laser) the fluorescent dye is excited. Part of the laser light is absorbed (energy) and, in turn, part of the absorbed energy is spontaneously re-emitted causing fluorescence. PLIF is a two-dimensional technique, the laser light is a sheet. A CCD camera is used to detect the emitted fluorescence signal and to provide an instantaneous spatial distribution of the dye concentration/temperature across the imaged area of the flow field [43][51]. The sketch of the PLIF arrangement is practically equal to that showed for PIV arrangement (Figure 3.3), the main difference is that in PLIF technique the fluorescence intensity is recorded instead of tracer particles.

The PLIF technique for analysing concentration in non-reactive flows can be extended to measure concentration in an acid-base reactive flow using a pH-dependent dye (see section 3.2.2.1). The concentration of the reactive species can be measured using the dependence of the fluorescence dye on the pH [1][52], see Section 3.2.3.

The pH-dependence of the dye can be used to measure either reactants or product in an acid-base reaction. If the dye is added to the acid and it is injected into a base, the dye is “turns on” by the increased pH produced by the acid-base reaction. In this case, the concentration of the product can be measured. On the other hand, if the dye is added to the base and it is injected into an acid, the dye is “turns off” allowing the measurement of reactants concentration.

3.2.2.1. Properties of pH-Dependent Dye

The pH-dependent dye used in this work is the sodium fluorescein ($C_{20}H_{12}O_5$). It has peak absorption (excitation) at wavelength around 490 nm. The emission occurs at the wavelength around 515 nm. Figure 3.8 shows the absorption and emission of sodium fluorescein [53].

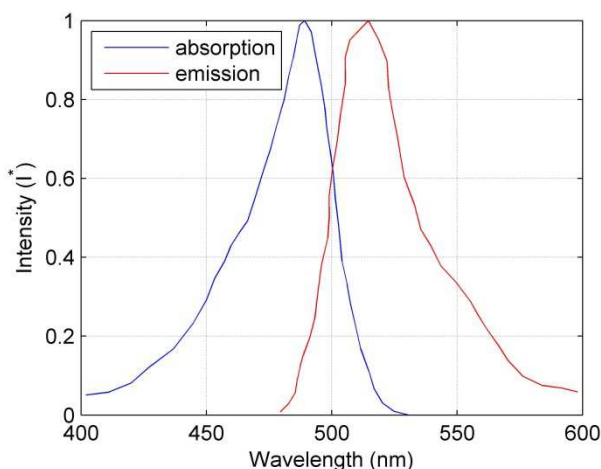


Figure 3.8. Absorption and emission wavelength of sodium fluorescein.

3.2.3. Simultaneous PIV and PLIF Techniques

The simultaneous application of PIV and PLIF techniques, allows the obtaining the velocity and the concentration fields of the flow at the same time. Figure 3.9 shows the experimental setup for simultaneous PIV and PLIF techniques.

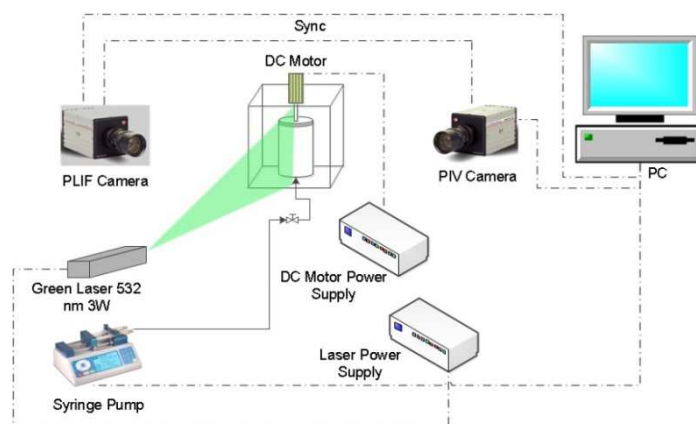


Figure 3.9. Sketch of the experimental setup of simultaneous PIV/PLIF experiments.

The PIV technique is used to estimate the velocity fields and the PLIF technique to estimate the concentration fields of the flow [50][51][54]. As it has been mentioned in section 3.2.2.1, the fluorescent dye used is sodium fluorescein which it is a pH dependent dye, so its fluorescent intensity changes along neutralization reaction allowing the determination of the instantaneous concentration using a calibration, see Figure 3.10.

For the calibration, the acid solution with the dye is added to the base solution until the equivalence point is reached, i.e. the mols of acid equal the mols of base. The light intensity for different values

of the molar fraction of base is shown in Figure 3.10a and the corresponding values of pH are plotted in Figure 3.10b. It can be seen that the maximum of intensity is observed at $x_B = 0.57$ (pH ≈ 8). For $x_B < 0.57$ the data have been fitted with an exponential function (red line) and for $x_B \geq 0.57$ zone with a second order polynomial (green line). In the present analyses, the concentration fields are estimated using the calibration at $x_B \geq 0.57$, because the acid-base reaction is studied in the early stages when, in most of the visualized section of the cylindrical cavity, the local molar fraction of base is in the range $x_B \geq 0.57$. It should be noted that, according to Figure 3.10a, a single value of intensity corresponds to two different values of molar fraction of base and that the quantitative determination of the concentration of base has to be restricted to regions in which the base is in excess ($x_B \geq 0.57$).

In order to calculate the concentration of the product (C_C^*) the Equation 3.4 [1] is used. A base molar fraction (x_B) of 0.57 corresponds to the maximum product concentration ($C_{C,\max}$) that can be experimentally measured. On the other hand, a base molar fraction (x_B) of 1 corresponds to no product concentration ($C_{C,0}$).

$$C_C^* = \frac{C_{C,i}}{C_{C,\max}} = \frac{I_i - I_b}{I_{\max} - I_b} \quad (3.4)$$

where C_C^* is the normalized concentration of the product (C+D), $C_{C,i}$ is the instantaneous concentration of the product and $C_{C,\max}$ is

the maximum concentration of the product that can be measured experimentally. In this case it corresponds to $x_B = 0.57$. I_i is the instantaneous intensity in grayscale, I_{\max} is the maximum intensity in grayscale which occurs for $x_B = 0.57$, and I_b is the background intensity in grayscale.

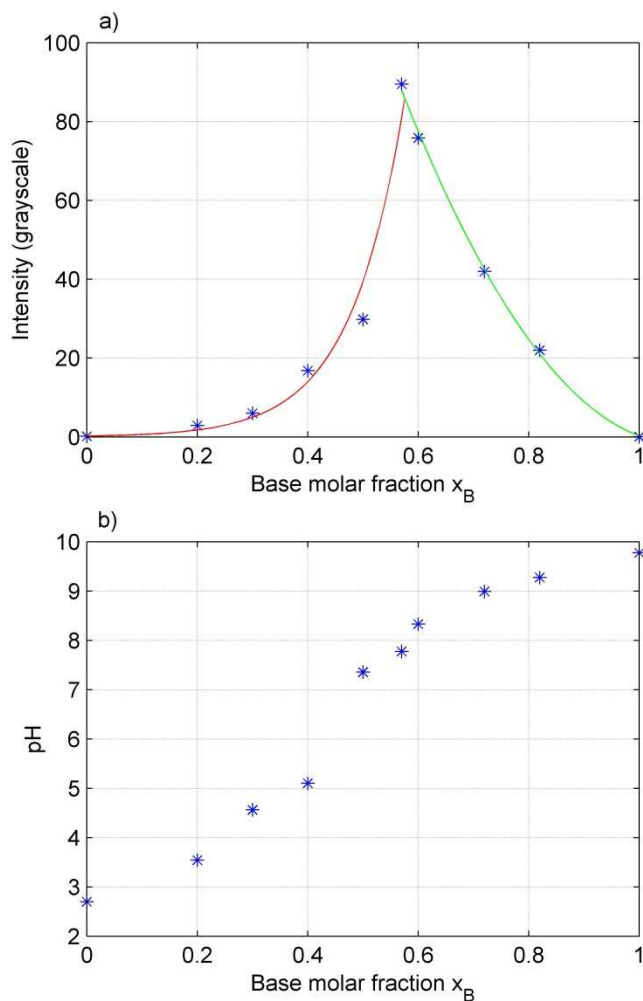


Figure 3.10. Calibration of PLIF technique. a) Titration of acid solution + dye in a base solution. b) pH of the solution during the titration.

It can be seen in Figure 3.10b that the pH of the equivalence point has a value between 7 and 8 which corresponds to base molar fraction (x_B) of 0.57. In previous studies [1] the base molar fraction corresponding to this equivalence point is 0.50. In our case, the glycerine modifies the pH of the solution; therefore the equivalence point is displaced.

The PLIF and PIV images are recorded using MotionPro X3 and MotionPro HS-3 cameras, respectively. The two digital cameras face each other. The laser is placed creating an angle of 90° with respect the two cameras, see Figure 3.9. The images are synchronized recorded at 200 frames per second corresponding to 800×800 pixels window size. A filter of 550 nm is added to the PLIF camera to remove from the images the particles and to obtain only the dye fluorescence, see Figure 3.11.

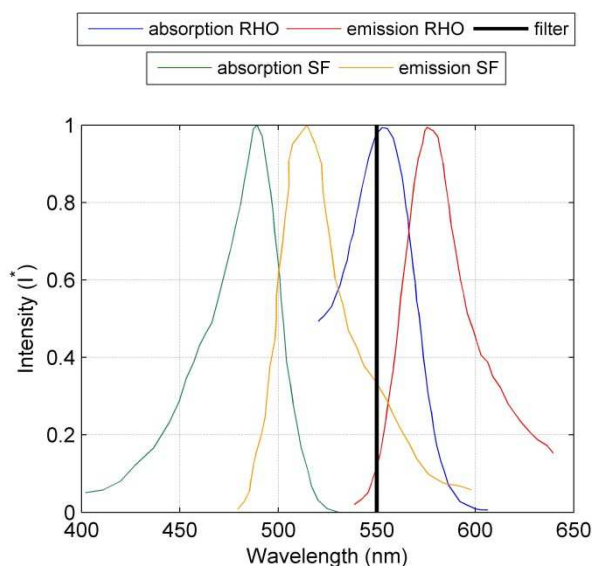


Figure 3.11. Absorption and emission wavelength of rhodamine (RHO) and sodium fluorescein (SF) dyes with the 550 nm filter.

The PIV camera records both, the dye fluorescence intensity and the light emitted by the particles functionalized with rhodamine. The fluorescence of the PIV image is removed from the images by subtracting the PLIF image from the PIV image. Figure 3.12 shows examples of the original PIV and PLIF images and the corresponding images after post-process.

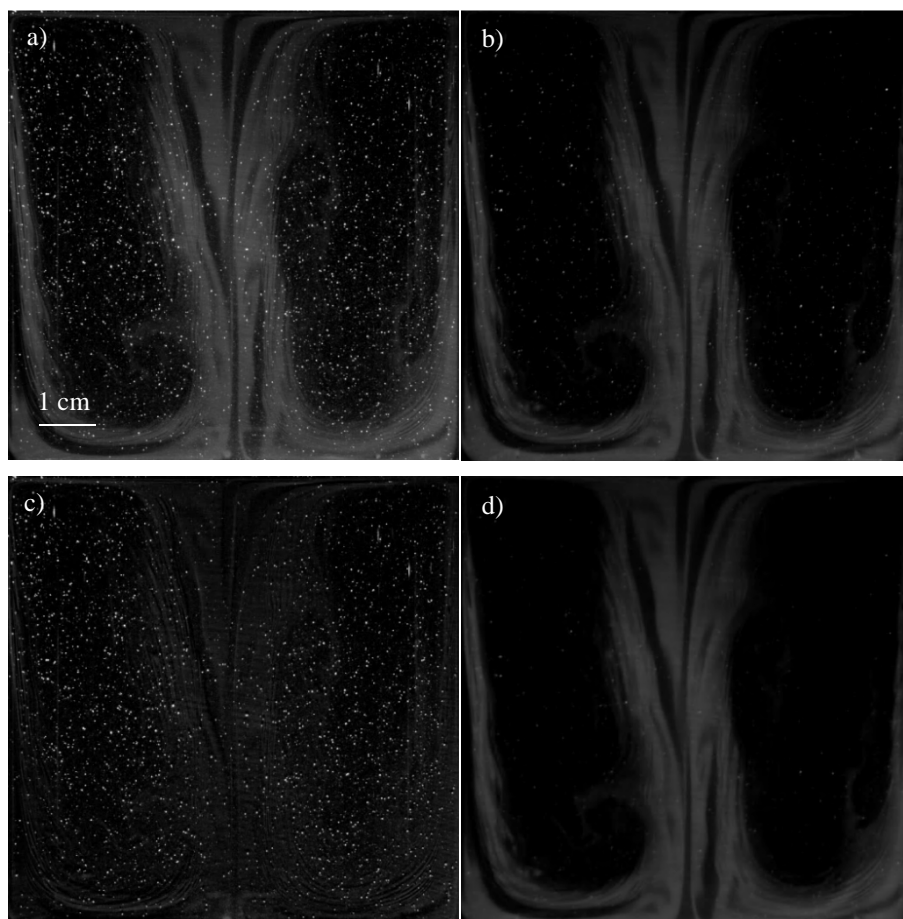


Figure 3.12. PIV and PLIF images at $Re = 1000$ and $t = 10$ min. a) Original PIV image with particles and signal of sodium fluorescein dye. b) Original PLIF image, with some particles. c) Treated PIV image, after post-processing. d) Treated PLIF image clean of particles and with only sodium fluorescein dye.

3.3. Numerical Simulation

The governing equations assuming incompressible flow with constant physical properties are:

$$\rho \frac{D\vec{V}}{Dt} = -\vec{\nabla}P + \mu \nabla^2 \vec{V} \quad (3.5)$$

$$\frac{DC_A^*}{Dt} = D_A \nabla^2 C_A^* - K_1 C_A^* C_B^* \quad (3.6)$$

$$\frac{DC_B^*}{Dt} = D_B \nabla^2 C_B^* - K_2 C_A^* C_B^* \quad (3.7)$$

The constants K_1 and K_2 are, respectively, $K_1 = KC_{B,0}$ and $K_2 = KC_{A,IN}$, where K is the kinetic constant of the reaction ($K = 10^8 \text{ m}^3/\text{mol}\cdot\text{s}$). C_A^* and C_B^* are defined as $C_A^* = C_A/C_{A,IN}$ and $C_B^* = C_B/C_{B,0}$, respectively. ρ is the density of the fluid ($\rho = 1100 \text{ kg/m}^3$) and D_A and D_B are, respectively, the diffusivity of acid and base solution ($D_A = 1.2 \cdot 10^{-9} \text{ m}^2/\text{s}$ and $D_B = 6.9 \cdot 10^{-9} \text{ m}^2/\text{s}$). C_A and C_B are the concentration of acid and base solution (mol/m^3), respectively. $C_{A,IN}$ is the concentration of the acid solution in the inlet (100 mol/m^3). $C_{B,0}$ is the initial concentration of the base solution in the cavity (10 mol/m^3).

The simulations have been performed with the finite volume commercial code Ansys Fluent v14.0 [55]. The SIMPLEC scheme

is chosen for the Pressure-Velocity coupling. The spatial discretization for gradient is least squares cell based and for pressure and momentum is second order. The equations solved for the two reactants are considered using defined scalars with their source terms added with user-defined functions, as defined in Equation 3.6 and Equation 3.7.

The critical Reynolds number for the boundary layer over a rotating disk is about $Re = 3 \cdot 10^5$ [56]. In the experiments, the Reynolds number is relatively low for all cases, from $Re = 1000$ to $Re = 2300$, so a laminar stationary solution is first computed for momentum and transient solutions are computed for concentrations. The velocity fields are computed until the results are converged. In the case of concentration fields, the second order unsteady forms of the discretized equations are solved with a time step of 0.1 seconds for all cases. Simulations with a time step of 0.05 seconds show a very similar time evolution of the results; see section 3.3.2.

3.3.1. Mesh Independence Test

A mesh independence test with three different meshes has been carried out. The meshes are formed by hexahedrons and have boundary layers attached to the walls and around the inlet, see Figure 3.13 and Table 3.1. Figure 3.14a shows the vertical velocity component profile (w^* , $w^* = w/\omega R$) along x -direction at $z^* = 0.375$ ($z^* = z/H$) and $y^* = 0$ ($y^* = y/R$) and at $Re = 2300$ for different grids. Figure 3.14b shows the profile of concentration

of B along z -direction at $x^* = 0.750$ ($x^* = x/R$) and $y^* = 0$ at the same Reynolds number. It can be seen that mesh 2 and mesh 3 give very similar results and therefore results have been computed with mesh 2.

Table 3.1. Boundary layers (BL) parameters.

	First row (mm)	Grow factor	Number of rows	Depth (mm)
BL along z - direction	0.1	1.2	18	12.8117
BL cylinder center	0.1	1.1	25	9.83471
BL top and bottom wall	0.2	1.1	18	9.11983

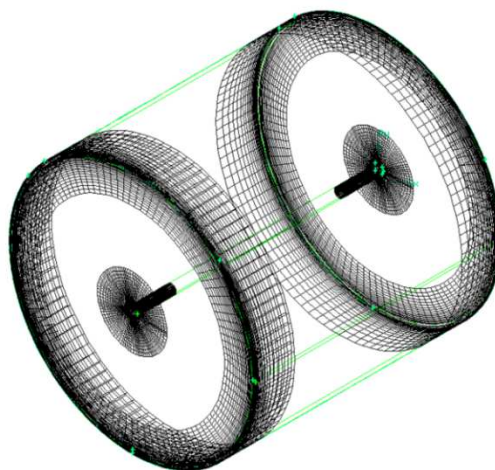


Figure 3.13. Sketch of the boundary layers (BL) used in the meshes. There are three zones: the BL along z -direction, the BL in the center of the cylinder and the BL in the top and bottom walls.

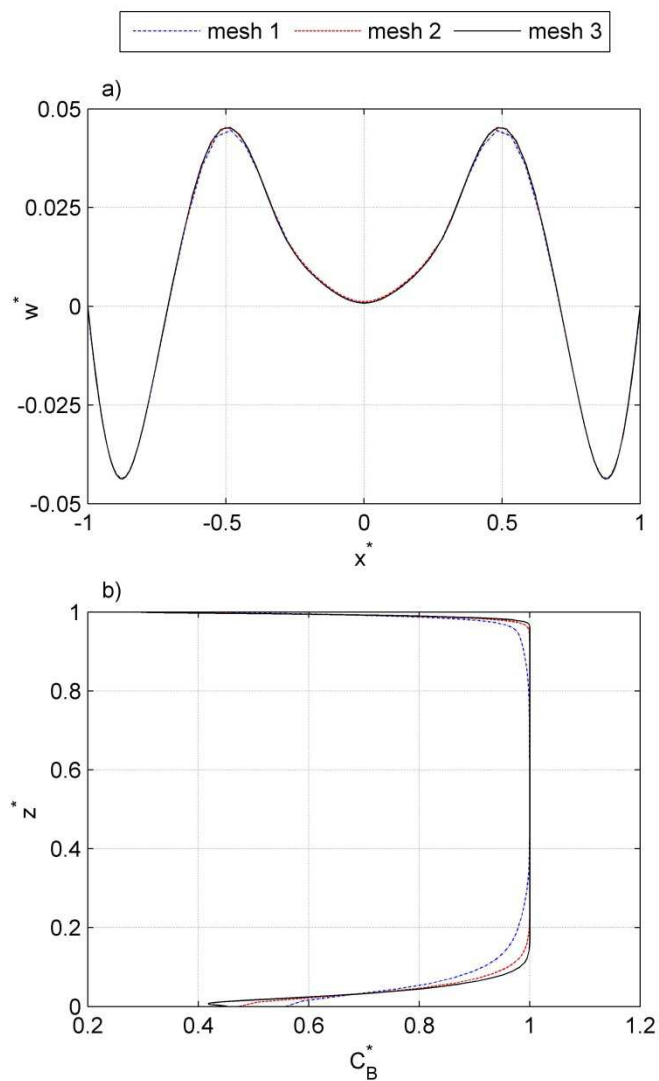


Figure 3.14. Mesh independence test at $Re = 2300$. Mesh 1: 0.36 Mnodes, mesh 2: 0.68 Mnodes and mesh 3: 0.92 Mnodes. a) Mesh independence test of velocity profiles along x -axis at $z^* = 0.375$. b) Mesh independence test of base concentration along the height of the cavity at $x^* = 0.750$ and $y^* = 0$.

3.3.2. Time Step Independence Test

A time step independence test with two different time steps has been carried out. Figure 3.15 shows the concentration of base solution profile (C_B^*) along z -direction at $x^* = 0.750$ and $y^* = 0$ and at $Re = 2300$ at different time step size. It can be seen that $tss = 0.10$ seconds and $tss = 0.05$ seconds give very similar results and therefore results have been computed with $tss = 0.10$ seconds.

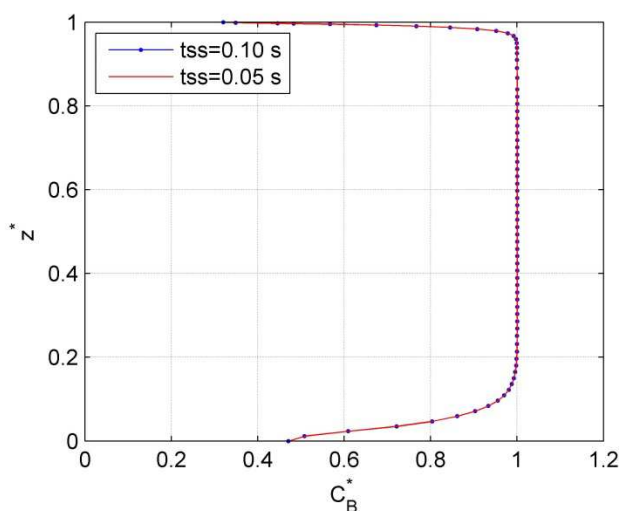


Figure 3.15. Time step size (tss) independence test at $Re = 2300$. Concentration of base solution profile (C_B^*) along z -direction at $x^* = 0.750$ and $y^* = 0$.

3.3.3. Acid Solution Inlet Analysis

The analysed flow is considered confined, although the cylindrical cavity has a bottom inlet. To ensure that the flow can be considered confined, the effect of the velocity inlet in the flow behaviour is analysed. Figure 3.16 shows the axial velocity (w^*) at $y^* = 0$ and at

different z^* positions of the cylindrical cavity at $Re = 1000$ when the flow is confined ($v_{IN} = 0$ m/s) and when there is a bottom inlet ($v_{IN} = 0.0032$ m/s). As it can be observed, the only difference it is noted at $z^* = 0$. Therefore, it can be considered that the flow is confined even it has a bottom inlet.

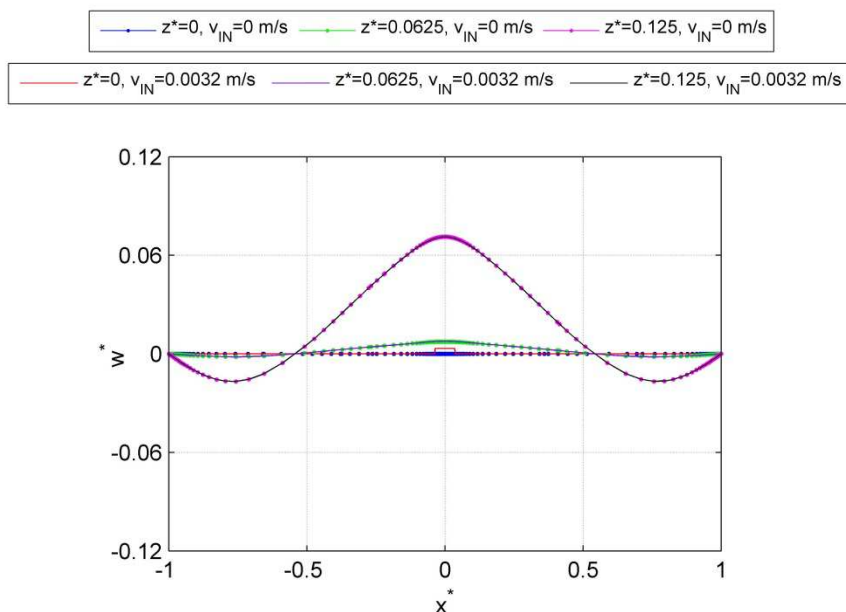


Figure 3.16. Analysis of the effect of the bottom inlet at $Re = 1000$. Axial velocity (w^*) at $y^* = 0$ at different z^* positions of the cylindrical cavity.

3.4. Flow Stabilization Time

Before starting the velocity and concentration measurements, it is required to estimate the time needed to achieve the steady state of the flow inside the cylindrical cavity. Figure 3.17 shows the experimental axial velocity (w^*) along x -axis at $Re = 1500$ and at $z^* = 0.25$. It can be seen that the steady state is reached at 5

minutes. From this time, the acid solution begins to be introduced to the cylindrical cavity.

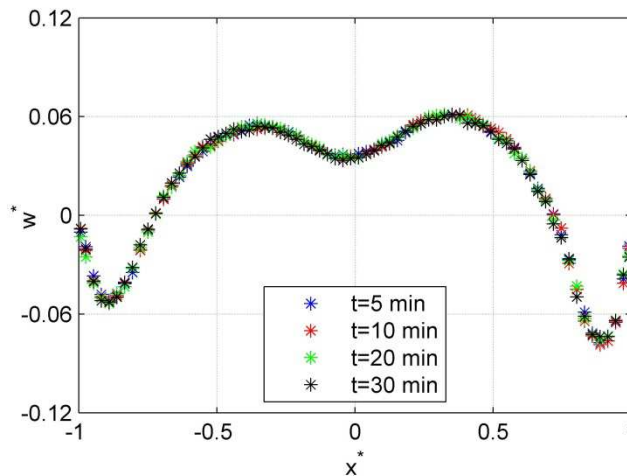


Figure 3.17. Analysis of the time required to achieve the steady state at

$Re = 1500$ and at $z^* = 0.25$.

3.5. Velocity Measurements

In this section the numerical and experimental velocity profiles at vertical and horizontal planes are analysed and compared with previous results [16][47]. Figures 3.18a and 3.18b show the measured secondary flows in a vertical plane of the cavity. This secondary flow, superimposed to the main rotating flow, has a three-dimensional toroidal shape. At low Reynolds number ($Re = 1000$, Figure 3.18a) there is a central viscous core which increases in diameter with decreasing distance from bottom endwall. As the rotation rate is increased, it is found the emergence of vortex breakdown bubbles. For example it can be seen in Figure 3.18b that the secondary flow field at $Re = 2300$ has a stagnation

point upstream of a zone of near stagnant recirculating fluid, which corresponds to a vortex breakdown bubble. The emergence of the first vortex breakdown for $H/R = 2$ occurs experimentally at $Re = 1450$ according to [16] and at $Re = 1474$ according to [47]. Figures 3.18c to 3.18g show the experimental and the numerical results of the axial velocity (w^*) at the cylinder axis ($x^* = 0, y^* = 0$). The number of vortex breakdown bubbles can be identified considering the number of stagnation points ($w^* = 0$) in each profiles. In agreement with the observations in [16] and [47], Figure 3.18d shows that at $Re = 1500$ occurs the first emergence of a vortex breakdown with a single bubble, located around $z^* \sim 0.4$. At $Re = 1700$ (Figure 3.18e) there is a single bubble located at similar position. At $Re = 2000$ (Figure 3.18f) the axial velocity profile shows two bubbles, the bottom one at $z^* \sim 0.2$ and the top one at $z^* \sim 0.5$. The stability diagram reported by Escudier [16] for $H/R = 2$ shows that $Re = 2300$ is a critical Reynolds number in which there is a transition between one and two bubbles in the vortex breakdown region. Figure 3.18g corresponding to this Reynolds number shows that experiments and simulations agree in the occurrence of a clearly identified bubble, located at $z^* = 0.2$ and a weaker bubble located around $z^* \sim 0.5$. In summary, Figure 3.18 shows that the velocity measurements are in general agreement with the numerical predictions and that the different flow structures of the secondary flows found at different Reynolds numbers agree with those reported in the literature [16].

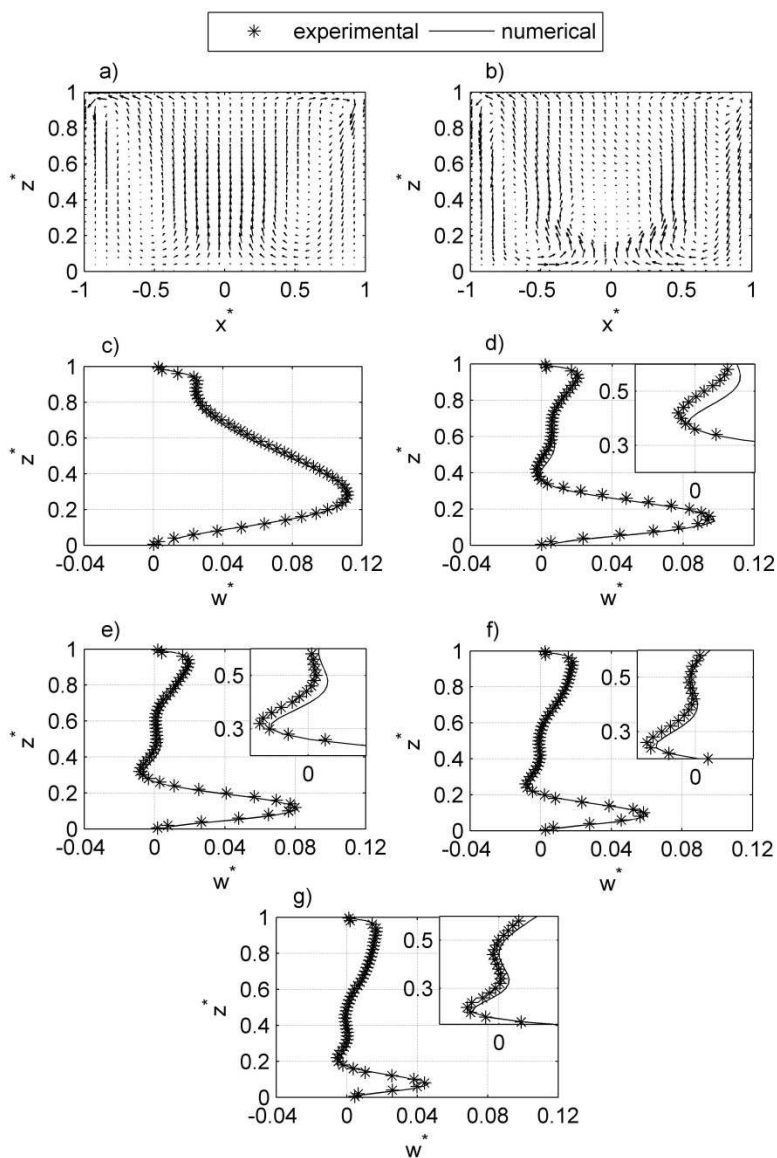


Figure 3.18. Velocity plots at different Reynolds number a) $Re = 1000$ and b) $Re = 2300$. Experimental and numerical results of the axial velocity (w^*) at the cylinder axis ($x^* = 0$ and $y^* = 0$). c) $Re = 1000$, d) $Re = 1500$, e) $Re = 1700$, f) $Re = 2000$ and g) $Re = 2300$.

The experimental and numerical velocity profiles of the vertical velocity component (w^*) at different axial positions (z^*) of the cavity are plotted in Figure 3.19. As it can be observed, when the vortex breakdown occurs, the velocity at the center of the cavity decreases (compare for example Figures 3.19a and 3.19c). Also, it can be noticed that the experimental velocities next to the cylindrical wall of the cavity, around $x^* = 0.9$ and $x^* = -0.9$, are not perfectly symmetric with respect to the axis of the cavity ($x^* = 0$). This phenomenon is analysed in section 3.6. However, it can be seen that the experimental velocity profiles are in general agreement with the numerical profiles and that even the asymmetry the behaviour of the vortex breakdown is reproduced numerically and experimentally.

The measured flow in the horizontal plane $z^* = 0.5$ is shown in Figure 3.20a. Figure 3.20b shows a good agreement between the present numerical results and the numerical predictions reported in [47] computed with the open source code Caffa3d.MB at $Re = 1500$ and $z^* = 0.375$. The comparison between the present experimental and numerical results of the velocity (v^* , $v^* = v/\omega R$) along the radial direction ($y^* = 0$, indicated in Figure 3.20a) is shown in Figure 3.20c. As it can be seen, the numerical and experimental results are in agreement in the lower half of the cavity ($z^* = 0.50$ and $z^* = 0.25$) and some differences are observed at $z^* = 0.75$, close to the rotating wall.

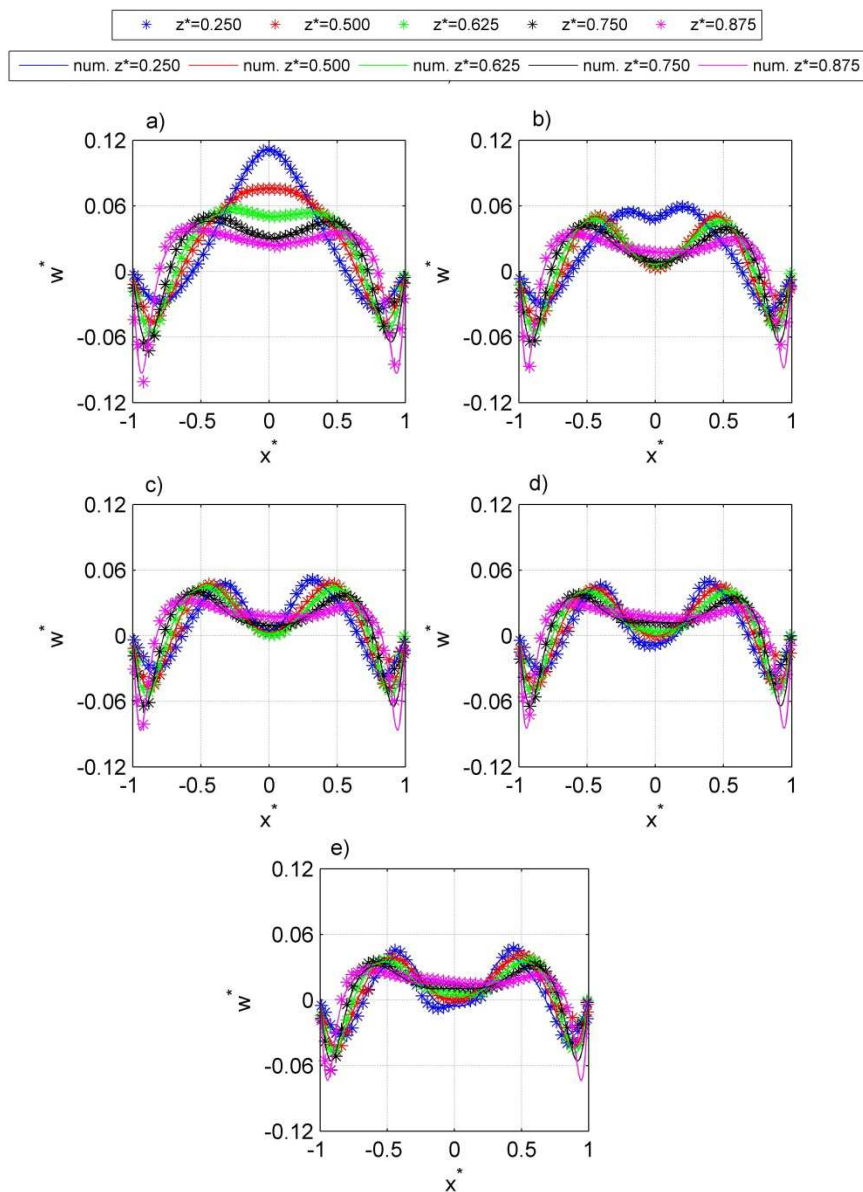


Figure 3.19. Experimental and numerical axial velocity (w^*) profiles at different axial positions (z^*) of the cylindrical cavity at $y^* = 0$. a) $Re = 1000$, b) $Re = 1500$, c) $Re = 1700$, d) $Re = 2000$ and e) $Re = 2300$.

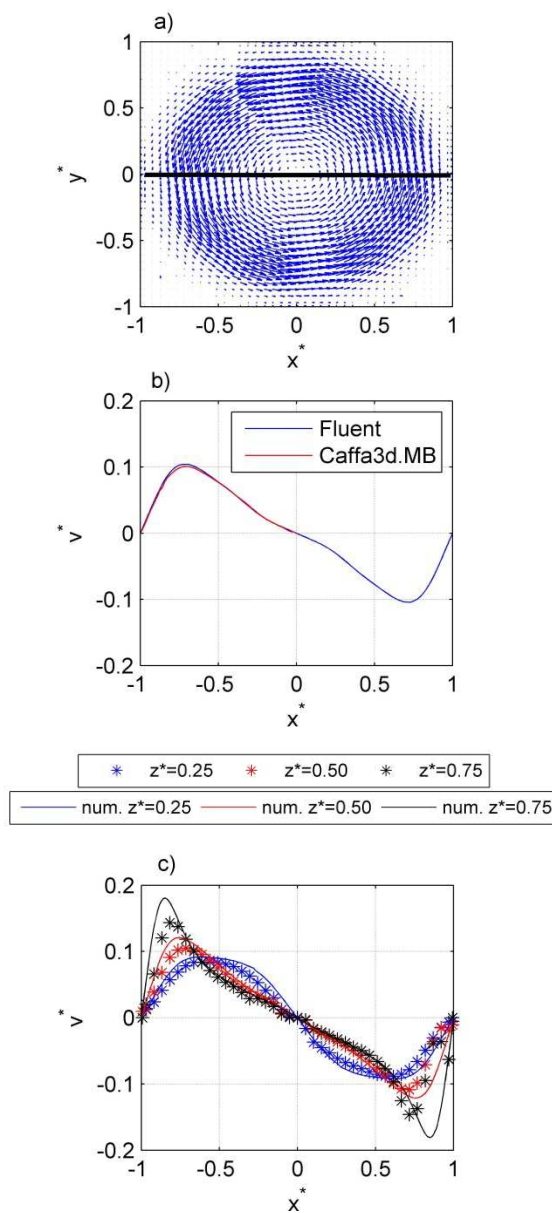


Figure 3.20. The flow in the horizontal plane at $Re = 1500$. a) In-plane velocity fields at $z^* = 0.500$. b) Comparison between numerical results of Fluent and Caffa3d.MB [47] of velocity profiles (v^*) at $z^* = 0.375$ and $y^* = 0$. c) Experimental and numerical velocity profiles (v^*) at different axial positions (z^*) of cylindrical cavity at $y^* = 0$.

3.6. Simultaneous Velocity and Concentration Measurements

The combination of PIV and PLIF techniques allows the simultaneous measurement of the velocity and concentration fields of the fluid within the illuminated plane of the flow.

The simultaneous application of the PIV and PLIF techniques allows the measurement of velocity profiles which are comparable to the velocity profiles acquired by only PIV (Figure 3.19). Figure 3.21 shows the comparison between the experimental axial velocity (w^*) along x -direction at different Reynolds numbers using only the PIV technique and using simultaneously the PIV and PLIF techniques. As it can be observed, the results are comparable and show that the PIV technique does not lose effectiveness when it is combined with PLIF.

Figure 3.22 shows the numerical contours of concentration of acid (C_A^*) (Figures 3.22a-1 to 3.22a-5), base (C_B^*) (Figures 3.22bn-1 to 3.22bn-5) and product (C_C^*) (Figures 3.22c-1 to 3.22c-5) at the central plane ($y^* = 0$), at time $t = 10$ minutes, for the different Reynolds numbers analysed. The experimental contours of concentration of base shown in Figures 3.22be-1 to 3.22be-5 have been obtained from the PLIF images using Equation 3.4 to obtain the nondimensional concentration of product and assuming that the concentration of acid (C_A^*) is negligible in comparison with the base

and product. Under this hypothesis the non-dimensional concentration of base can be computed as,

$$C_B^* = 1 - C_C^* \quad (3.8)$$

Figures 3.22a-1 to 3.22a-5 show the numerical contours of concentration of the acid solution (C_A^*). It can be seen that the acid is located along the axis of the cylindrical cavity. In the cases with vortex breakdown bubbles (Figures 3.22a-2 to 3.22a-5) the acid enters and reacts inside the vortex breakdown region. The numerical predictions of the base concentrations (Figures 3.22bn-1 to 3.22bn-5) show large values in the cores of the large secondary flows and low values along the axis of the cylinder. The distribution of the product (Figures 3.22c-1 to 3.22c-5) is vice versa (i.e. low values in the cores and large values along the axis) supporting the approximation adopted in Equation 3.8.

Figures 3.22bn-1 to 3.22bn-5 and Figures 3.22be-1 to 3.22be-5 show, respectively, the numerical and experimental contours of concentration of the base solution (C_B^*). A general view shows that the experimental contours of concentration (Figures 3.22be-1 to 3.22be-5) have small-scale mixing layers that are not observed in the numerical simulations (Figures 3.22bn-1 to 3.22bn-5) and that the experimental results show some asymmetries, with respect the axis of the cylinder that are discussed afterward.

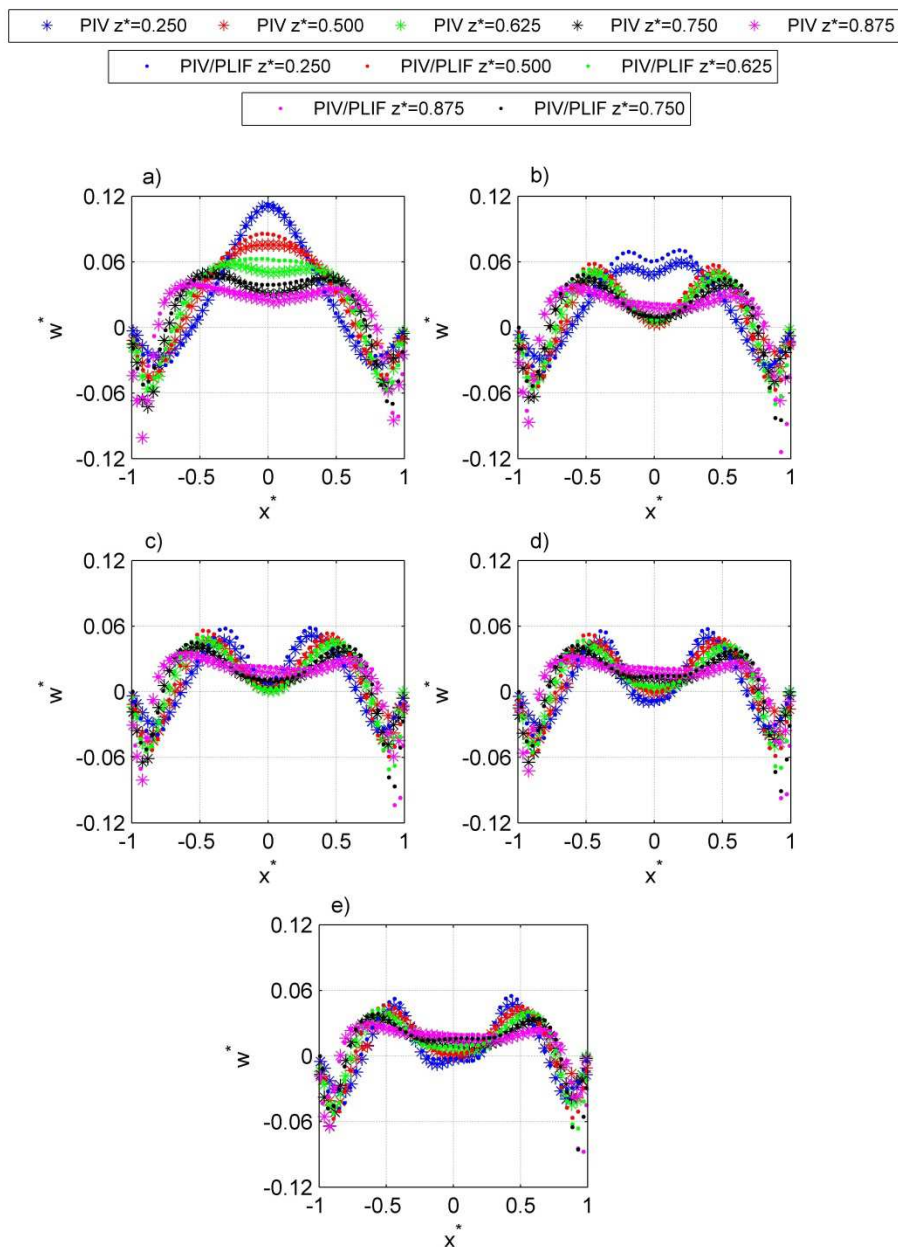


Figure 3.21. Comparison between only PIV and PIV/PLIF experimental velocity profiles (w^*) at different axial position (z^*) of the cylindrical cavity at $y^* = 0$ at a) $Re = 1000$, b) $Re = 1500$, c) $Re = 1700$, d) $Re = 2000$ and e) $Re = 2300$.

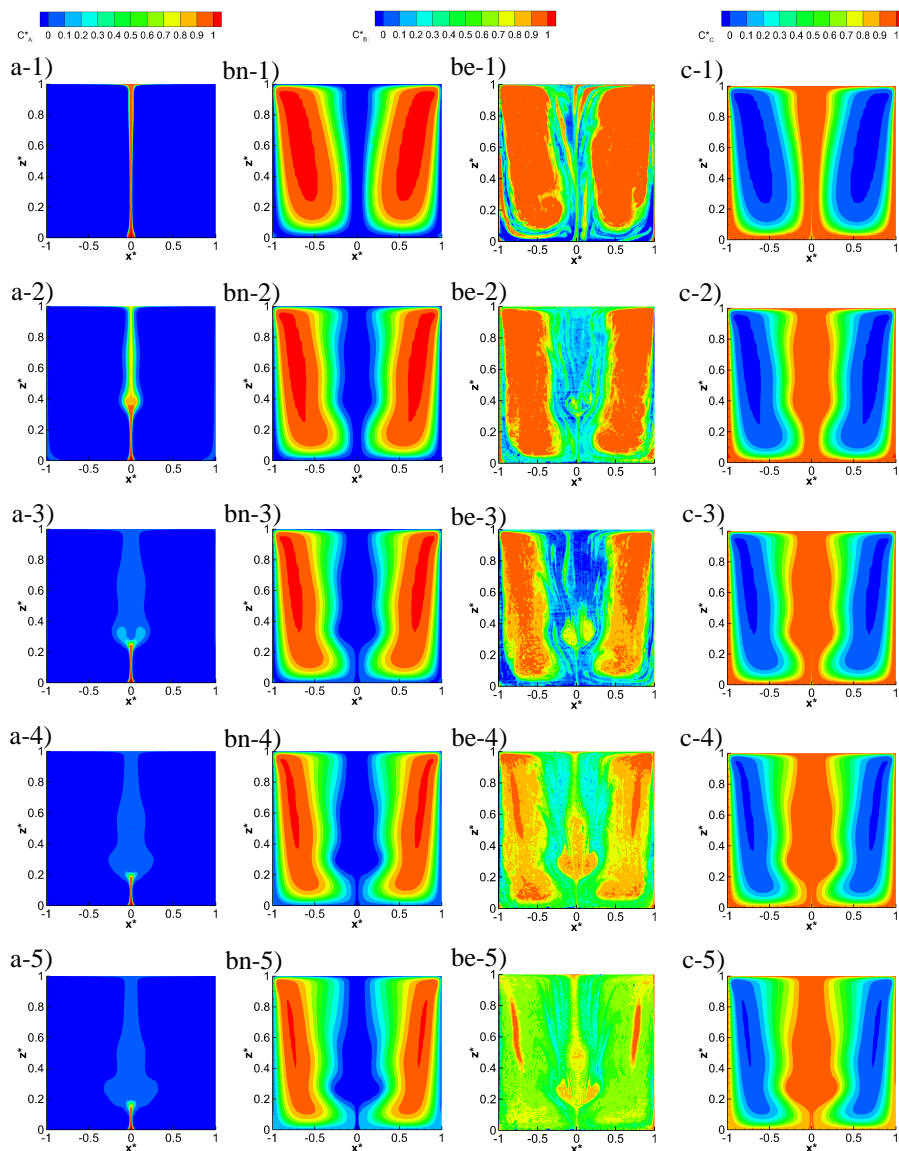


Figure 3.22. Experimental and numerical contours of concentration of acid (C_A^*),

base (C_B^*) and product (C_C^*) solution at center plane ($y^* = 0$) at $t = 10$ min at

1) $Re = 1000$, 2) $Re = 1500$, 3) $Re = 1700$, 4) $Re = 2000$ and 5) $Re = 2300$.

a-1) to a-5) Numerical contours of concentration of acid solution.

bn-1) to bn-5) Numerical contours of concentration of base solution.

be-1) to be-5) Experimental contours of concentration of base solution.

c-1) to c-5) Numerical contours of concentration of product solution.

Focusing on the results at $Re = 1000$, 1500 and 1700 (Figures 3.22bn-1 to 3.22bn-3 and Figures 3.22be-1 to 3.22be-3), the numerical and the experimental contours of concentration of base are in general agreement. However, at $Re = 1700$ the experimental contours of concentration (Figure 3.22be-3) show at the center of the vortex breakdown region two symmetrically distributed maxima of the concentration which are not observed in the numerical contours of concentration (Figure 3.22bn-3). A similar phenomenon occurs at $Re = 2000$ and 2300 (Figures 3.22be-4 and 3.22be-5, respectively) where the numerical and experimental concentration of base inside the vortex breakdown bubbles differ. It should be noted that the relation between the intensity and the concentration of base (Figure 3.10a) indicates that a single value of intensity corresponds to two molar fractions of base. It can be seen that the numerical and experimental concentrations agree in the core of the large-scale toroidal recirculation where the base is in excess and, consequently, Equation 3.4 is applicable. However, at $t = 10$ minutes the base has been consumed inside vortex breakdown bubbles, where the numerical simulations indicate that the concentration of product is large, and in these regions Equation 3.4 is not applicable.

To analyse this, the numerical contours of intensity have been obtained and compared with the experimental ones, obtained directly from the PLIF images. To compute the numerical contours of intensity the experimental calibration shown in Figure 3.10a is used to determine the intensity for each numerical value of the molar fraction. Figure 3.23 shows the experimental and the

numerical contours of intensity at $y^* = 0$ and at different Reynolds numbers analysed. Figures 3.23b-1 to 3.23b-5 show the numerical contours of intensity obtained from the contours of Figures 3.22bn-1 to 3.22bn-5. It can be seen that the numerically computed intensity inside the vortex breakdown predicts a low intensity region as in the PLIF images (Figure 3.23a-1 to 3.23a-5).

To determine the effect of small imperfections of the experimental setup on the flow and concentration, simulations with a lateral displacement in the axis of rotation of the top wall have been performed. Figure 3.24 shows the numerical contours of intensity for lateral displacements ($\Delta x/2R$) of the axis of rotation at $Re = 2000$ and 2300 . As it can be seen, a relatively small deviation has an important impact in the flow in the vortex breakdown region, as reported by Brøns *et al.* [23]. Specifically, the interface between the low intensity region of the core of the large-scale toroidal recirculation (with $x_b \geq 0.57$) and the low region intensity of the vortex breakdown bubble (with $x_b < 0.57$) appears more blurred, as in the experimental PLIF image (Figures 3.23a-4 and 3.23a-5), in comparison to the numerical prediction without displacement of the rotating axis (Figure 3.23b-4 and 3.23b-5). It seems that the most similar numerical contours of intensity in comparison with the experimental contours of intensity (Figures 3.23a-4 and 3.23a-5) are those have a lateral displacement of $\Delta x/2R = 2.5 \cdot 10^{-2}$ (Figure 3.24b-1 and 3.24b-2).

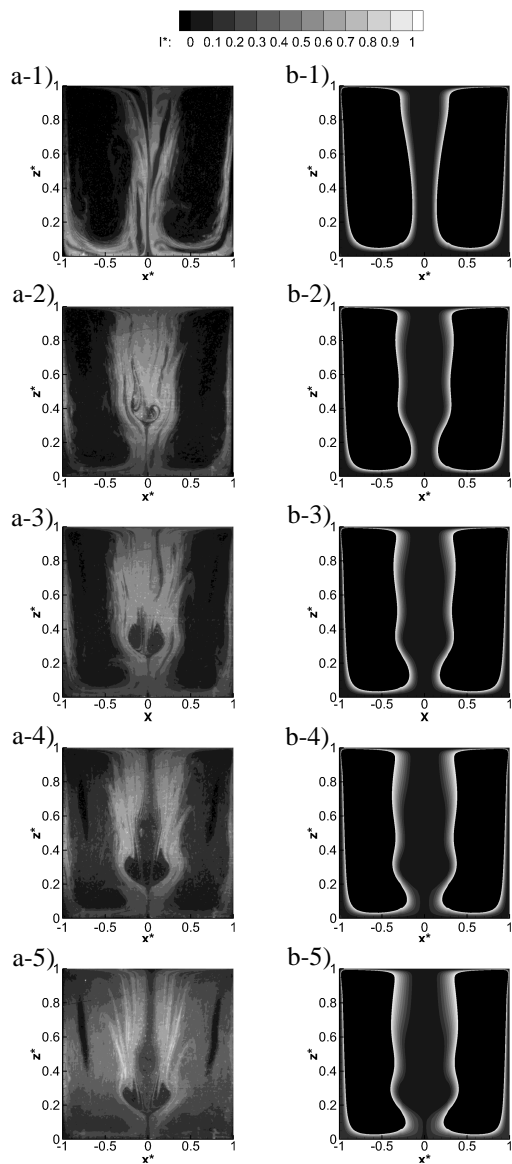


Figure 3.23. Experimental and numerical contours of intensity (I^*) at
 1) $Re = 1000$, 2) $Re = 1500$, 3) $Re = 1700$, 4) $Re = 2000$ and 5) $Re = 2300$.
 a-1) to a-5) Experimental contours of intensity. b-1) to b-5) Numerical contours
 of intensity.

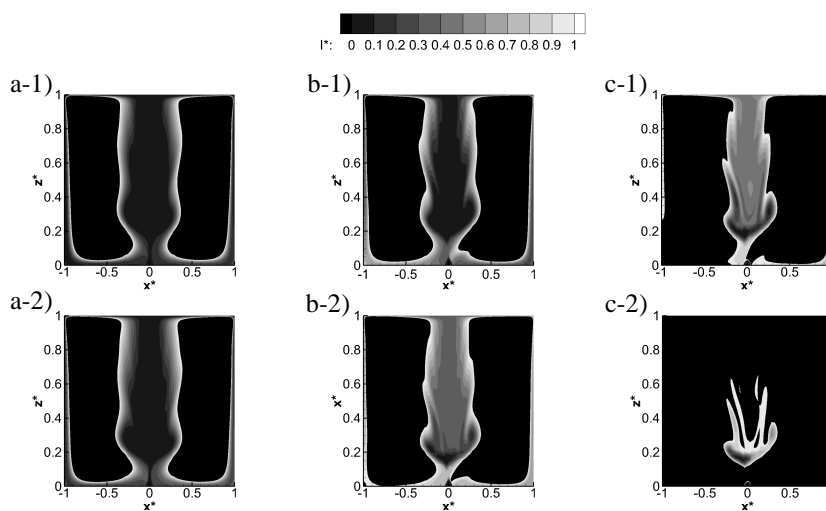


Figure 3.24. Numerical contours of intensity (I^*) with a lateral displacement in the axis of rotation of the top wall at different Reynolds numbers, 1) $Re = 2000$

and 2) $Re = 2300$. a-1) and a-2) Displacement of $\Delta x/2R = 1.25 \cdot 10^{-2}$.

b-1) and b-2) Displacement of $\Delta x/2R = 2.50 \cdot 10^{-2}$. c-1) and c-2) Displacement of

$\Delta x/2R = 3.75 \cdot 10^{-2}$.

To illustrate the effect of the displacement of the rotating axis with respect to the axis of the cylinder, Figure 3.25 shows the experimental velocity profiles using simultaneously PIV and PLIF techniques and corresponding numerical profiles with a displacement in the rotation axis at $Re = 2000$ and 2300 . It can be observed, that the numerically introduced asymmetry improves the agreement between the simulations and experiments shown in Figure 3.19. This indicates that small, totally unavoidable, imperfections of the experimental setup can be the cause of the asymmetry detected on the velocity profiles and on the PLIF images, as well as, of the small-scale mixing layers observed in the PLIF images.

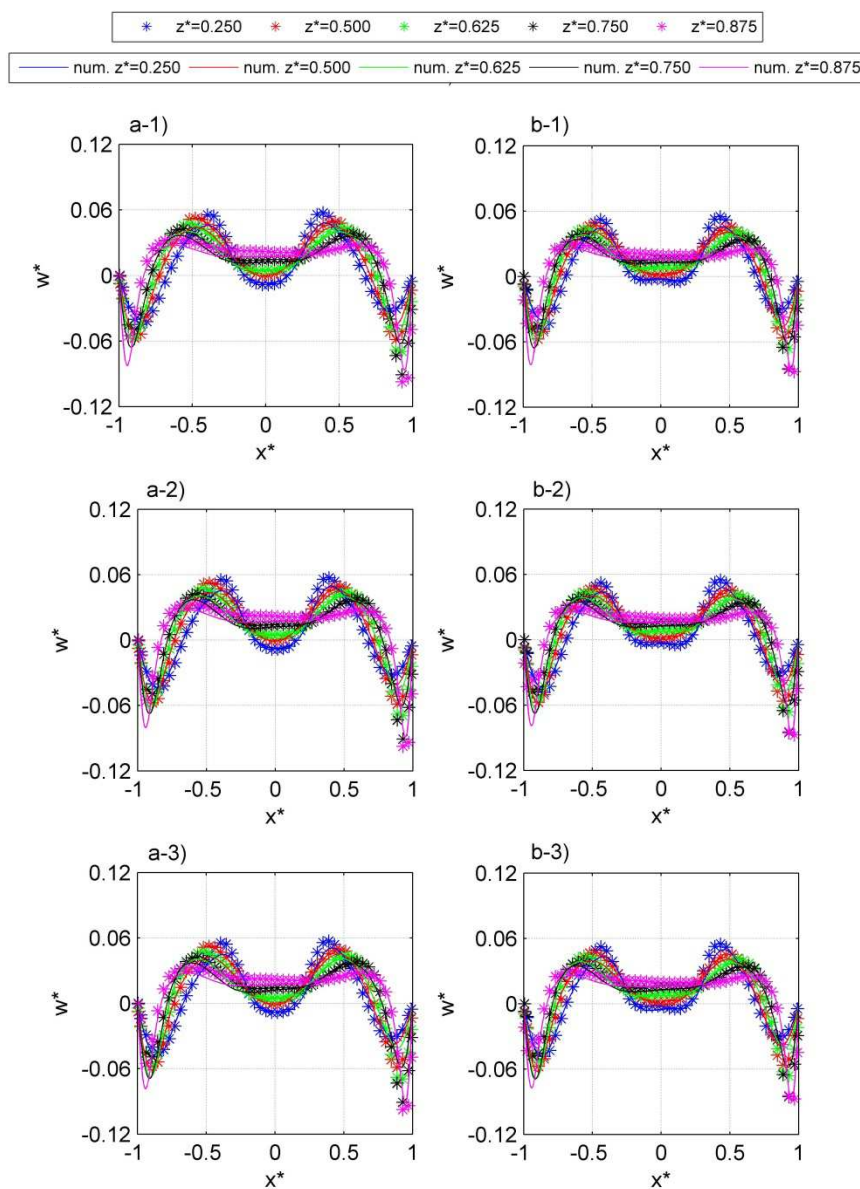


Figure 3.25. Experimental and numerical velocity profiles (w^*) at different axial positions (z^*) at $y^* = 0$ adding a displacement in the axis of the rotating wall of

1) $\Delta x/2R = 1.25 \cdot 10^{-2}$, 2) $\Delta x/2R = 2.50 \cdot 10^{-2}$ and 3) $\Delta x/2R = 3.75 \cdot 10^{-2}$ at

different Reynolds numbers a) $Re = 2000$ and b) $Re = 2300$.

To analyse the effect of the flow on the chemical reaction, the time evolutions of the numerically obtained volume-averaged non-dimensional product concentration ($\overline{C_C^*}$) and its standard deviation ($\overline{\sigma}$) are plotted in Figure 3.26. The standard deviation is defined as:

$$\overline{\sigma} = \int_V \frac{\sqrt{(C_C - C_{C,ideal})^2}}{C_{C,ideal}} dV \quad (3.9)$$

where the C_C is the instantaneous local concentration of product and $C_{C,ideal}$ is the instantaneous theoretical concentration of product corresponding to a perfectly mixed reactor. Note that in a perfectly mixed situation $\overline{\sigma} = 0$.

It can be seen in Figures 3.26a and 3.26b that the rate of product production and the uniformity of the concentration of product increase with the Reynolds number. Three different values of the lateral displacement of the axis of rotation ($\Delta x/2R$) at $Re = 2000$ are considered. Figure 3.26 shows that, for the fast irreversible chemical reaction considered, the small lateral displacements essentially improve the uniformity of concentrations and, thus, the mixing, as also suggested by the comparison of Figures 3.24a-1, 3.24b-1 and 3.24c-1.

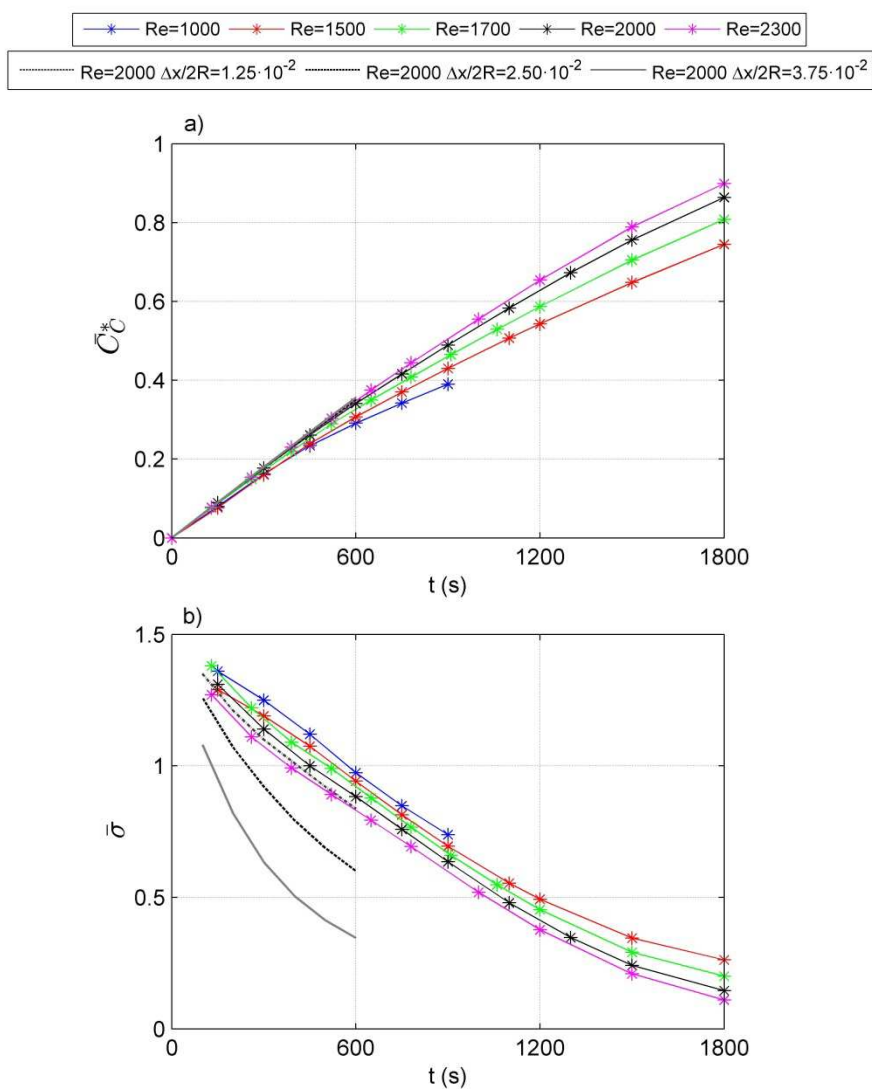


Figure 3.26. Time evolutions of a) the volume averaged nondimensional product concentration ($\overline{C_C^*}$) and of b) the volume averaged standard deviation ($\overline{\sigma}$) of the product concentration.

3.7. Conclusions

In this chapter an axisymmetric, confined, reactive and laminar flow in a cylindrical cavity with a rotating endwall has been analysed

experimentally and numerically. A basic solution is initially in the cavity and an acid solution is introduced at very low velocity through the center of the stationary endwall when the flow in the cavity is at the steady state. In the range of Reynolds number considered $1000 \leq \text{Re} \leq 2300$ the flow and the concentration distribution have been measured simultaneously using a combined PIV/PLIF technique. The numerical simulations and the PIV measurements of the flow are in agreement with results available in the literature. It has been found that the measurement of the velocity fields using the simultaneous combination of the PIV and PLIF techniques does not show loss of effectiveness in comparison with measurements using only the PIV technique. The PIV/PLIF technique allows the simultaneous measurement of the velocity field and the visualization of the concentration distribution of the base within an illuminated plane of the flow. The quantitative measurement of the concentration of the base can be performed in the regions where the base is in excess (specifically at $x_B \geq 0.57$). In this range the intensity of the fluorescein decreases quasi-linearly with the concentration of base. At lower concentrations the intensity decreases sharply making the measurement of the concentration of base difficult because of the relatively low intensity levels.

It has been observed that at low Reynolds number ($\text{Re} = 1000$) there is a central viscous core which increases in diameter with decreasing distance from bottom endwall. As the rotation rate is increased, it is found the emergence of vortex breakdown bubbles. The experimental visualization of the concentration fields have been

compared with the numerical results. At $Re = 1000$ and 1500 , the numerical and experimental contours of concentration show a general a good agreement. At larger Reynolds numbers, $Re = 1700$, 2000 and 2300 , the concentration of base inside the bubbles is reduced because of the introduction, by the flow, of the acid in the vortex breakdown region. In these regions and under these conditions, the quantitative measurement of the concentration of base and the direct comparison with the simulations is not feasible. However, the synthetic images of the intensity obtained using the numerically predicted concentration distributions show a similar flow pattern as that revealed by the experimental images.

The effect of small displacements of the rotating axis of the wall with respect to the cylinder axis has been analysed numerically. It has been found that the asymmetries observed experimentally in the velocity profiles and in the contours of concentration can be explained considering this effect in the experimental setup. Numerical simulations of the flow show that small displacements of the axis of rotation have a noticeable effect on the mixing of the chemicals inside the cavity.

Chapter 4

4. Particle Deposition on the Wall of a Microchannel for Enzymatic Reactions

In this chapter, the magnetic particles deposition rate on the wall of a straight microchannel is analysed. The particles deposition is induced by a permanent magnet. Two different types of magnetic particles are tested: SPHERO™ Carboxyl Magnetic and Dynabeads® M-270 Carboxylic Acid. The SPHERO™ are paramagnetic particles and are prepared by coating a layer of magnetite and polystyrene onto monodispersed polystyrene core particles [32]. Dynabeads® are uniform, monosized superparamagnetic particles coated with a hydrophilic layer of glycidyl ether, followed by further coating with carboxylic acid groups [34]. It is reported the morphology of the particles cluster that deposit on the microchannel wall at different flow rates. This study addresses experimental and numerical aspects of the particles deposition.

4.1. Experimental Setup

The experimental setup consists in a thiol-ene [27][28] microchannel with a length $L = 0.04$ m. The microchannel has a square section of $5 \cdot 10^{-4} \times 7 \cdot 10^{-5}$ m ($W \times D_m$). Figure 4.1 shows the sketch of the microchannel. The coordinate system is located at

point O . The analysed solution is a mixing between deionized water and magnetic particles solution with a volume concentration of 1%. The properties of the two types of particles tested are shown in Table 4.1. The solution is introduced inside the microchannel with a syringe pump (Nanojet Chemix), operating at inlet velocities between $v_{IN} = 0.00238-0.02381$ m/s, corresponding to volumetric flow rate between $Q_v = 0.005-0.050$ mL/min. The microchannel has a free outlet. The magnetic particles are deposited on the wall of the microchannel using a magnet. The permanent magnet is a cube of 5 mm [57] and its center is situated at $x = 0$ m and $y = 3 \cdot 10^{-3}$ m, see Figure 4.1. The analysis of the particles deposition is made with a microscope ($\times 10$ lens) which has installed a digital camera (MotioCam 2300 3.0M Pixels). Figure 4.2 shows a picture of the microchannel.

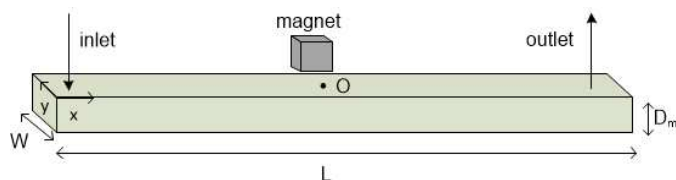


Figure 4.1. Sketch of the experimental setup. The dimensions of the microchannel

are $L \times W \times D_m = 4 \cdot 10^{-2} \times 5 \cdot 10^{-4} \times 7 \cdot 10^{-5}$ m.

Table 4.1. Properties of magnetic particles.

Magnetic particles	Diameter (μm)	N_{beads} (beads/mL)	ρ (g/mL)	N_{beads} in 0.1 mL solution
SPHERO™	1.14	$\sim 2.04 \cdot 10^{10}$	1.58	$\sim 2.04 \cdot 10^7$
Dynabeads®	2.80	$\sim 2 \cdot 10^9$	0.03	$\sim 2 \cdot 10^6$

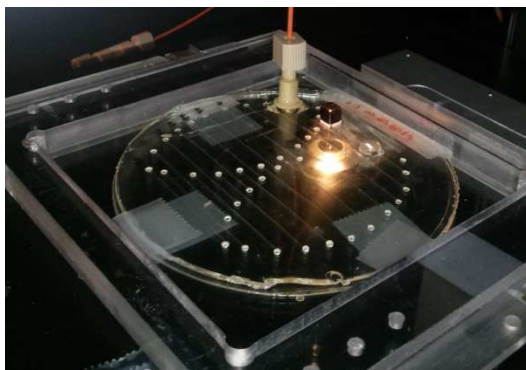


Figure 4.2. Picture of the microchannel with the permanent magnet.

The volume of the solution introduced in the microchannel is 0.1 mL. Therefore, the number of magnetic beads introduced in the microchannel is also known, see Table 4.1. When the total volume has been introduced in the microchannel, the digital camera takes images of the deposited particles. To estimate the number of particles deposited on the walls of the microchannel due to the magnetic field created by the permanent magnet; the images taken by the digital camera are treated with Matlab to compute the area of the deposited particles. It is assumed that every black pixel in the image is a magnetic particle. This method is accurate because the resolution of the images (1280×1024 pixel) is enough as if to each magnetic particle only takes up a pixel. Once the area occupied by the deposited particles is computed, the number of the deposited particles can be calculated knowing the size of each particle, see Table 4.1. The number of deposited particles is computed with Equation 4.1:

$$\% \text{ wall deposition particles} = \frac{P_D}{P_T} \cdot 100 \quad (4.1)$$

where P_D are the particles deposited on the wall of the microchannel and P_T are the total particles introduced in the microchannel, see Table 4.1.

4.2. Numerical Simulation

The governing equations, assuming incompressible flow with constant physical properties, are the continuity (Equation 4.2) and the momentum (Equation 4.3) equations [58]:

$$\vec{\nabla} \cdot \vec{u} = 0 \quad (4.2)$$

$$\frac{\partial \vec{u}}{\partial t} + (\vec{u} \cdot \vec{\nabla}) \vec{u} = -\frac{1}{\rho} \vec{\nabla} P + \nu \nabla^2 \vec{u} + \frac{\vec{F}_v}{\rho} \quad (4.3)$$

where \vec{u} is the velocity vector (m/s), ρ is the density of the fluid ($\rho = 998 \text{ kg/m}^3$), P is the pressure (Pa), ν is kinematic viscosity of the fluid (m^2/s) and \vec{F}_v is the volume force vector (N/m^3).

The electromagnetic analysis on a macroscopic level is solved with the Maxwell's equations. In this case, it is assuming a quasi-static analysis of the magnetic and electric fields which is valid under the assumption that $\partial D_e / \partial t = 0$. This implies that it is possible to rewrite Maxwell's equations in the following manner [59]:

$$\vec{\nabla} \times \vec{H}_m = \vec{J} = \sigma_e (\vec{E} \times \vec{v}_e \times \vec{B}_m) + \vec{J}_e \quad (4.4)$$

$$\nabla \times E = -\frac{\partial B_m}{\partial t} \quad (4.5)$$

$$\nabla \cdot B_m = 0 \quad (4.6)$$

$$\nabla \cdot D_e = \rho_e \quad (4.7)$$

$$\nabla \cdot J = 0 \quad (4.8)$$

Where E is the electric field intensity (V/m), D_e is the electric displacement or electric flux density (C/m²), H_m is the magnetic field intensity (A/m), B_m is the magnetic flux density (T), J is the current density (A/m²), ρ_e is the electric charge density (C/m³), σ_e is the electrical conductivity (S/m), J_e is an externally generated current density (A/m²) and v_e is the velocity of the conductor (m/s).

In this case, the magnetostatic fields to solve are free of electric current and it is possible to solve it using a scalar magnetic potential. In a current-free case $\nabla \times H_m = 0$. This implies that the magnetic scalar potential (V_m) can be defined from the relation $H_m = -\nabla V_m$, which is analogous to the definition of the electric potential for static electric fields. Using the consecutive relation $B_m = \mu_0(H_m + M)$, the equation $\nabla \cdot B_m = 0$ becomes:

$$-\nabla \cdot (\mu_0 \nabla V_m - \mu_0 M) = 0 \quad (4.9)$$

In planar 2D the dynamic formulation also involves the thickness d in the z -direction:

$$-\nabla \cdot d(\mu_0 \nabla V_m - \mu_0 M) = 0 \quad (4.10)$$

Where μ_0 is the permeability of free space ($\mu_0 = 4\pi \cdot 10^{-7} \text{ N/A}^2$), V_m is the magnetic scalar potential (A), M is the magnetization vector (A/m) and d is the thickness (m).

When the flow field (Equations 4.2 and 4.3) and the magnetic field (Equation 4.10) are solved, the particle tracing is analysed. The motion of a particle is defined by Newton's second law [60]:

$$m \frac{d^2 x}{dt^2} = F \left(t, x, \frac{dx}{dt} \right) \quad (4.11)$$

where x is the position of the particle (m), m the particle mass (kg) and F is the sum of all forces acting on the particle. In this case, the forces analysed are the drag force (F_D , Equation 4.12), the magnetic force (F_M , Equation 4.13) and the gravity force (F_g , Equation 4.14). The fluid dynamic drag will be predicted by Stokes law and the magnetophoretic force is based on the gradient magnetic field:

$$F_D = \frac{18\mu}{\rho_p d_p^2} m(u - u_p) \quad (4.12)$$

$$F_M = 2\pi r_p^3 \mu_0 \mu_{r,f} K_e \nabla H_m^2 \quad (4.13)$$

$$F_g = mg \frac{(\rho_p - \rho)}{\rho_p} \quad (4.14)$$

Where μ is the fluid dynamic viscosity ($\mu = 1 \cdot 10^{-3}$ Pa·s), ρ_p is the particle density (kg/m^3 , Table 4.1), d_p is the particle diameter (m, Table 4.1), u is the fluid velocity (m/s), u_p is the velocity of the particle (m/s), r_p is the particle radius (m, Table 4.1), μ_0 is the permeability in the free space ($\mu_0 = 4\pi \cdot 10^{-7}$ N/A²), $\mu_{r,f}$ is the fluid relative permeability ($\mu_{r,f} = 1$), $\mu_{r,p}$ is the particle relative permeability ($\mu_{r,p} = 1.05$), H_m is the magnetic field (A/m), g is the gravity vector ($g = 9.81$ m/s²), ρ is the fluid density ($\rho = 998$ kg/m³), m is the particle mass (kg) and K_e is defined as:

$$K_e = \frac{\mu_{r,p} - \mu_{r,f}}{\mu_{r,p} + 2\mu_{r,f}} \quad (4.15)$$

The particle-particle iteration is computed using the Lennard-Jones force in which is specified the interaction distance between the particles. In this case the interaction distance is set to the particle radius, see Table 4.1. The expression of this force on the i^{th} particle becomes:

$$F_l = \frac{24\epsilon}{\sigma_c} \sum_{j=1}^N \left[2 \left(\frac{\sigma_c}{|r_i - r_j|} \right)^{13} - \left(\frac{\sigma_c}{|r_i - r_j|} \right)^7 \right] \left(\frac{r_i - r_j}{|r_i - r_j|} \right) \quad (4.16)$$

where ε is the interaction strength ($\varepsilon = 1.6 \cdot 10^{-21}$ J, interaction between neutral particles), σ_c is the collision diameter ($\sigma_c = r_p = 5.70 \cdot 10^{-7}$ m), r_i is the position vector of the i^{th} particle (m) and r_j is the position vector of the j^{th} particle (m).

The simulations have been performed in 2D with the commercial code COMSOL Multiphysics 4.4, which is based on the Finite Elements Method. The velocity fields (Equation 4.2 and Equation 4.3) and the magnetic fields (Equation 4.10) are computed in stationary state. The particle tracing (Equation 4.11) is solved in time-dependent with a time step size of 0.01 seconds. The sketch of the geometry used in COMSOL is shown in Figure 4.3.

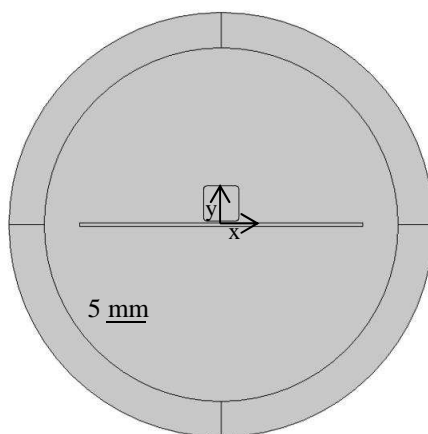


Figure 4.3. Sketch of the geometry in COMSOL Multiphysics 4.4. The rectangle represents the microchannel, the square represents the permanent magnet and the disk is the environment, needed to compute the magnetic fields in COMSOL

Multiphysics 4.4.

The superparamagnetic particles (Dynabeads®) have the capacity to reorient the magnetic moments, due to this property its numerical

simulation requires a great deal of computational time. Because of this, the numerical simulation analysis is focused in the paramagnetic particles (SPHERO™). The analysis of the deposition of the particles is done similarly to the experimental part (Equation 4.1). The number of introduced particles ($N_{beads} = 1000$) and the deposited particles are known analysing the numerical results.

4.2.1. Mesh Independence Test

A mesh independence test with three different meshes has been carried out. The mesh in the microchannel (rectangle showed in Figure 4.3) and in the external disk (Figure 4.3) is a mapped mesh. The rest of geometry has a triangular mesh. Figure 4.4a shows the velocity magnitude in the center of the microchannel ($y = 0$ m) along x -direction at inlet velocity $v_{IN} = 0.02381$ m/s. In Figure 4.4b, it can be seen, the magnetic flux density (B_m) in the center of the microchannel ($y = 0$ m) along x -direction at inlet velocity $v_{IN} = 0.02381$ m/s. It can be seen that mesh 1, 2 and 3 give very similar results. Therefore results have been computed with mesh 1.

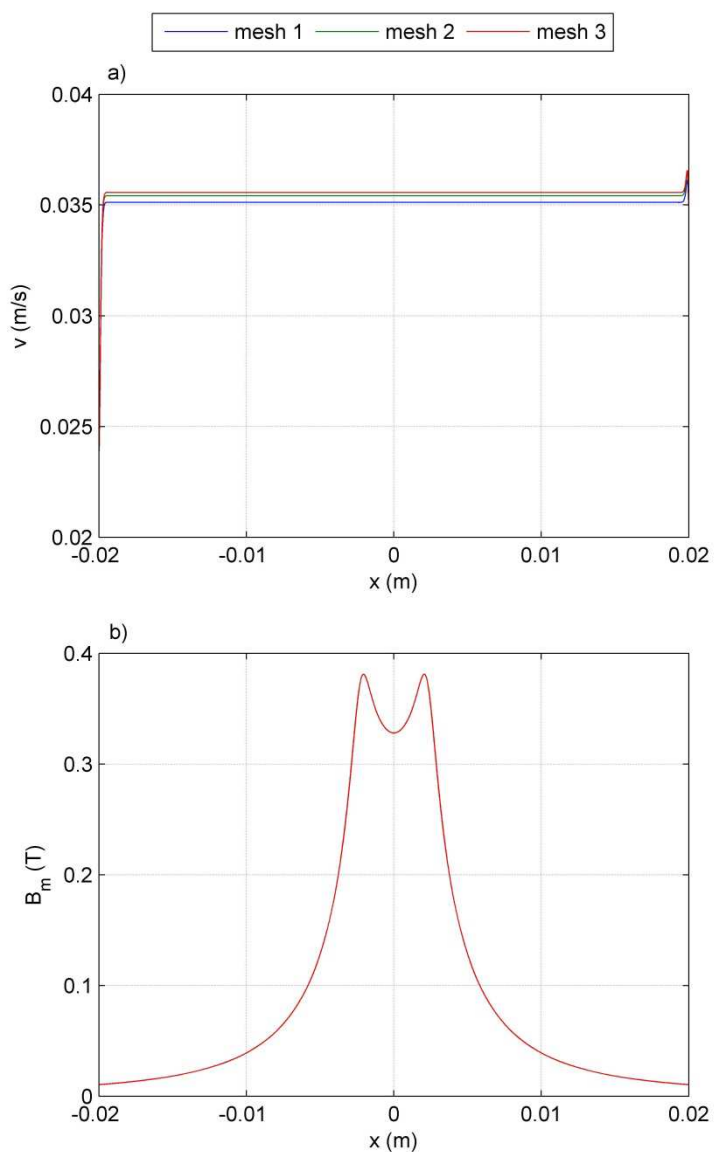


Figure 4.4. Mesh independence test at center of the microchannel ($y = 0$ m) along x -direction at $v_{IN} = 0.02381$ m/s. Mesh 1: 59380 nodes, mesh 2: 149590 nodes and mesh 3: 421010 nodes. a) Velocity magnitude. b) Magnetic flux density.

4.3. Results

In this section, the experimental and numerical results are shown. In the experimental analysis the deposition on the wall of the microchannel of the paramagnetic SPHERO™ particles and the superparamagnetic Dynabeads® particles is studied. In the numerical analysis the deposition is only analysed for the paramagnetic SPHERO™ particles.

4.3.1. Experimental Results

The images taken of the deposited particles on the wall of the microchannel after introducing the 0.1 mL of solution are shown in Figure 4.5 and Figure 4.6. Figure 4.5a shows the deposition of the Dynabeads® particles at $Q_v = 0.0100$ mL/min. As it can be observed the particles form chains, increasing the surface area of the beads more suitable, for example, for chemical reactions and enzymes immobilization. Figure 4.5b shows the particles behaviour when the magnet is removed. As it can be seen, the particles continue in the surroundings of the magnet but with higher distribution due to the diffusion. The behaviour of these particles is due to their superparamagnetic nature. Dynabeads® particles have the capacity to magnetize themselves and convert each particle in a permanent magnet. For this behaviour, their numerical simulation requires a lot of computational time. On the other hand, Figure 4.6 shows the deposition of the SPHERO™ particles at different volume flow rate. It can be observed that the higher volume flow rate the lower is the area occupied by the particles.

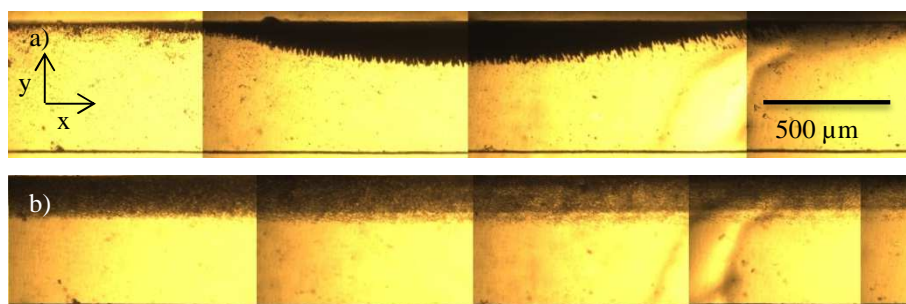


Figure 4.5. Images obtained from the experiments with Dynabeads® Carboxylic Acid beads. a) $Q_v = 0.0100$ mL/min. b) $Q_v = 0.0100$ mL/min removing the magnet.

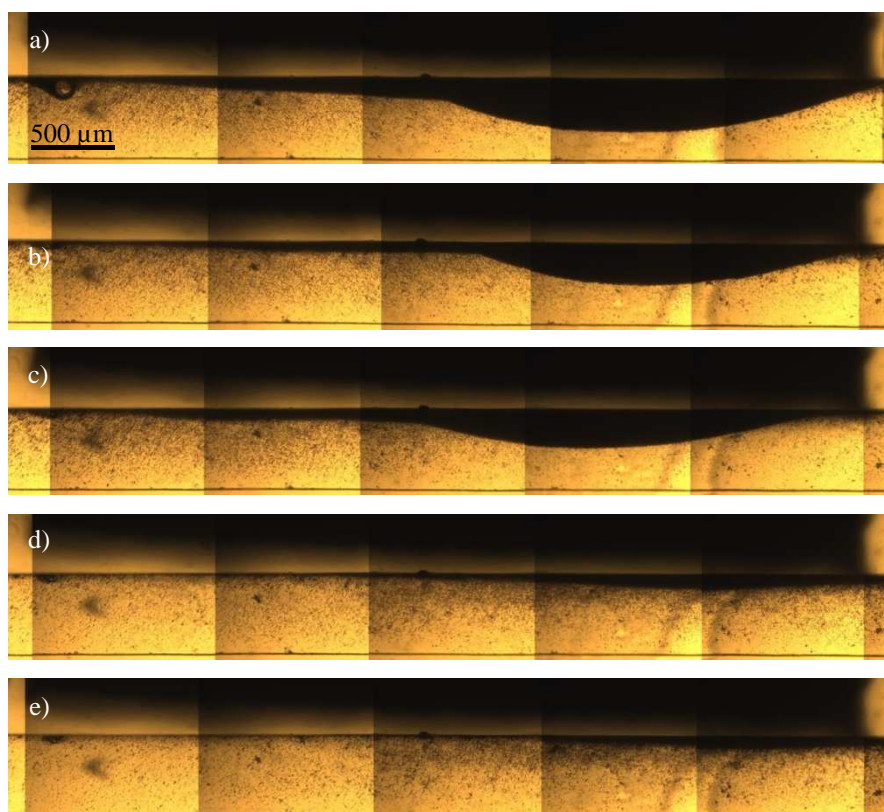


Figure 4.6. Images obtained from the experiments with SPHERO™ Carboxyl magnetic beads. a) $Q_v = 0.0050$ mL/min. b) $Q_v = 0.0075$ mL/min. c) $Q_v = 0.0100$ mL/min. d) $Q_v = 0.0250$ mL/min. e) $Q_v = 0.0500$ mL/min.

4.3.2. Numerical Results

The simulations have been done using the properties of SPHERO™ particles. Figure 4.7 shows the magnetic field produced by the permanent magnet. The magnetic field is the same for all different cases analysed ($Q_v = 0.0050$ - 0.0500 mL/min).

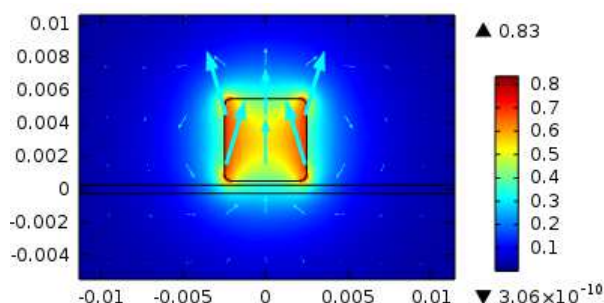


Figure 4.7. Magnetic flux density (B_m) produced by the permanent magnet.

Figure 4.8 shows the numerical particle tracking at different time at $Q_v = 0.0500$ mL/min. As it can be seen in Figure 4.8a, before the particles arrive to the magnet, the particles have a parabolic shape. Once they reach the magnet, some of them reduce the velocity due to the magnetic field depositing on the wall next to the magnet.

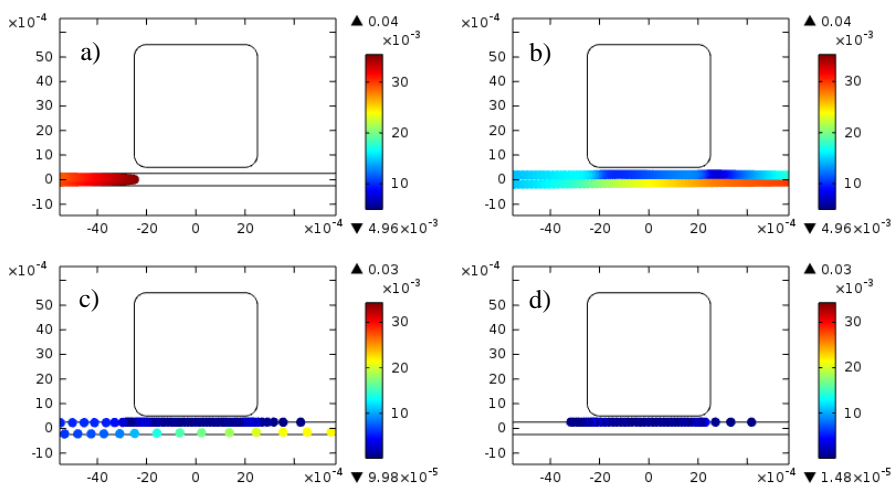


Figure 4.8. Numerical particle tracking at different time at $Q_v = 0.0500$ mL/min.

a) $t = 0.5$ s. b) $t = 1.0$ s. c) $t = 2.5$ s. d) $t = 5.0$ s.

4.3.3. Comparison between Experimental and Numerical Results

The experimental and numerical comparison between the number of particles deposited on the wall due to magnetic field can be seen in Figure 4.9. The comparison is made for SPHERO™ particles. It can be observed that the number of beads deposited on the wall of the microchannel decreases exponentially with the volume flow rate, both experimentally and numerically. Numerical results performed by COMSOL Multiphysics 4.4 overestimates the experimental results. This can be because of the accumulation of beads in the numerical simulation has not been possible to simulate and, therefore, the comparison between the numerical and experimental results is not totally accurate. Moreover the simulations have been carried out in 2D, underestimating the effect of the magnetic field in the z -direction.

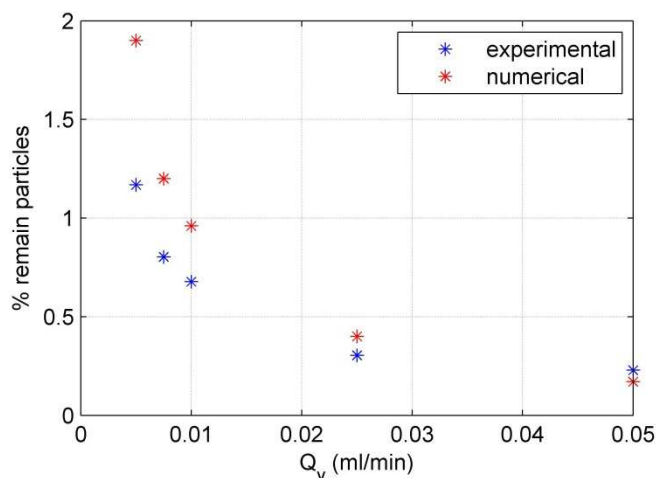


Figure 4.9. Comparison between experimental and numerical deposited particles (SPHERO™) on the wall of microchannel.

4.4. Conclusions

The wall deposition of the magnetic particles due to permanent magnet at different flow rate but constant volume has been analysed. Experimentally two different types of beads have been checked: SPHERO™ Carboxyl Magnetic particles and Dynabeads® Carboxylic Acid particles. The Dynabeads® are superparamagnetic particles and, therefore, have the ability to magnetize themselves becoming each particle as a permanent magnet. For this reason the quantitative study is focus on the SPHERO™ particles, since the numerical simulation of Dynabeads® particles has a high computational cost. Qualitatively the Dynabeads® particles have been analysed.

It can be observed that magnetic particles are accumulated in the surrounding of the permanent magnet creating a convex shape. In

the case of SPHERO™ particles the surface is smooth. However, due to its ability to magnetize them and create chains, the surface of the Dynabeads® particles is toothed, increasing its surface. The gain of surface area does Dynabeads® more convenient to, for example, immobilization of enzymes or chemical reactions.

In COMSOL Multiphysics 4.4, 2D numerical simulations with SPHERO™ particles properties are performed. The numerical results are not totally accurate, being that the numerical simulations are in 2D and, moreover, the accumulation of the particles has not been simulated, i.e. we only have information of the first line of particles.

The comparison between the experimental and numerical results has been carried out analysing the % of particle retained on wall due to the permanent magnet. It can be observed that the lower flow rate the higher deposition of the particles. The numerical and experimental results are only in agreement at the highest flow rates ($Q_v = 0.0250-0.0500$ mL/min). The numerical simulation at lower flow rates overestimates the number of particles deposited on the wall of microchannel.

This analysis shows preliminary results. Possible future points could be perform numerical simulations in 3D to study the effect of z -direction in the particles deposition. Moreover an interesting point to analyse would be developing enzyme reaction test setup for monitoring the enzyme activity on magnetics particles.

References

- [1] L. K. Hjertager Osenbroch, B. H. Hjertager, and T. Solberg, “Experiments and CFD modelling of fast chemical reaction in turbulent liquid flows,” *International Journal of Chemical Reactor Engineering*, vol. 3, pp. 1–30, 2005.
- [2] J. Bałdyga and R. Pohorecki, “Turbulent micromixing in chemical reactors — a review,” *The Chemical Engineering Journal and the Biochemical Engineering Journal*, vol. 58, no. 2, pp. 183–195, 1995.
- [3] J. Bałdyga and J. R. Bourne, *Turbulent mixing and chemical reactions*. Wiley, 1999.
- [4] J. Bałdyga and R. Pohorecki, “Turbulent micromixing in chemical reactors - a review,” *The Chemical Engineering Journal and The Biochemical Engineering Journal*, vol. 58, no. 2, pp. 183–195, 1995.
- [5] R. O. Fox, *Computational Models for Turbulent Reacting Flows*. Cambridge University Press, 2003.
- [6] H. Feng, M. G. Olsen, Y. Liu, R. O. Fox, and J. C. Hill, “Investigation of turbulent mixing in a confined planar-jet reactor,” *AIChE Journal*, vol. 51, no. 10, pp. 2649–2664, 2005.

- [7] A. Chorny and V. Zhdanov, “Turbulent mixing and fast chemical reaction in the confined jet flow at large Schmidt number,” *Chemical Engineering Science*, vol. 68, no. 1, pp. 541–554, 2012.
- [8] P. A. Libby and F. A. Williams, *Turbulent reacting flows*. London; New York: Academic Press, 1994.
- [9] L. K. Hjertager, B. H. Hjertager, and T. Solberg, “CFD modelling of fast chemical reactions in turbulent liquid flows,” *Computers & Chemical Engineering*, vol. 26, no. 4–5, pp. 507–515, 2002.
- [10] R. Pohorecki and J. Baldyga, “New model of micromixing in chemical reactors. 1. General development and application to a tubular reactor,” *Industrial and Engineering Chemistry Fundamentals*, vol. 22, no. 4, pp. 392–397, 1983.
- [11] J. Hannon, S. Hearn, L. Marshall, A. I. of C. Engineers, and A. I. of C. E. Meeting, *Assessment of CFD Approaches to Predicting Fast Chemical Reactions*. distributed by American Institute of Chemical Engineers, 1998.
- [12] A. Fabregat, J. Pallarès, I. Cuesta, and F. X. Grau, “Numerical simulations of a second-order chemical reaction in a plane turbulent channel flow,” *International Journal of Heat and Mass Transfer*, vol. 53, no. 19–20, pp. 4248–4263, 2010.

- [13] V. Zhdanov, N. Kornev, E. Hassel, and A. Chorny, “Mixing of confined coaxial flows,” *International Journal of Heat and Mass Transfer*, vol. 49, no. 21–22, pp. 3942–3956, 2006.
- [14] I. Sancho, A. Fabregat, J. Pallares, and A. Vernet, “Macro- and micromixing in a plane turbulent channel flow with a second-order chemical reaction,” *Computers & Fluids*, vol. 88, pp. 156–164, 2013.
- [15] C. Fukushima, L. Aanen, and J. Westerweel, “Investigation of the mixing process in an axisymmetric turbulent jet using PIV and LIF,” in *Laser Techniques for Fluid Mechanics*, Springer Berlin Heidelberg, 2002, pp. 339–356.
- [16] M. P. Escudier, “Observations of the flow produced in a cylindrical container by a rotating endwall,” *Experiments in Fluids*, vol. 2, no. 4, pp. 189–196, 1984.
- [17] J. M. Lopez, “Axisymmetric vortex breakdown Part 1. Confined swirling flow,” *Journal of Fluid Mechanics*, vol. 221, pp. 533–552, 1990.
- [18] G. L. Brown and J. M. Lopez, “Axisymmetric vortex breakdown Part 2. Physical mechanisms,” *Journal of Fluid Mechanics*, vol. 221, pp. 553–576, 1990.
- [19] J. M. Lopez and A. D. Perry, “Axisymmetric vortex breakdown. Part 3 Onset of periodic flow and chaotic advection,” *Journal of Fluid Mechanics*, vol. 234, pp. 449–471, 1992.

- [20] A. Y. Gelfgat, P. Z. Bar-Yoseph, and A. Solan, “Stability of confined swirling flow with and without vortex breakdown,” *Journal of Fluid Mechanics*, vol. 311, pp. 1–36, 1996.
- [21] A. Spohn, M. Mory, and E. J. Hopfinger, “Experiments on vortex breakdown in a confined flow generated by a rotating disc,” *Journal of Fluid Mechanics*, vol. 370, pp. 73–99, 1998.
- [22] F. Sotiropoulos and Y. Ventikos, “The three-dimensional structure of confined swirling flows with vortex breakdown,” *Journal of Fluid Mechanics*, vol. 426, pp. 155–175, 2001.
- [23] M. Brøns, W. Z. Shen, J. N. Sørensen, and W. J. Zhu, “The influence of imperfections on the flow structure of steady vortex breakdown bubbles,” *Journal of Fluid Mechanics*, vol. 578, pp. 453–466, 2007.
- [24] O. Lucca-Negro and T. O’Doherty, “Vortex breakdown: a review,” *Progress in Energy and Combustion Science*, vol. 27, no. 4, pp. 431–481, 2001.
- [25] C. Cabeza, G. Sarasúa, A. C. Martí, I. Bove, S. Varela, G. Usera, and A. Vernet, “Influence of coaxial cylinders on the vortex breakdown in a closed flow,” *European Journal of Mechanics - B/Fluids*, vol. 29, no. 3, pp. 201–207, 2010.
- [26] K. Hourigan, L. J. W. Graham, and M. C. Thompson, “Spiral streaklines in pre-vortex breakdown regions of axisymmetric swirling flows,” *Physics of Fluids*, vol. 7, no. 12, pp. 3126–3128, 1995.

- [27] T. M. Sikanen, J. P. Lafleur, M.-E. Moilanen, G. Zhuang, T. G. Jensen, and J. P. Kutter, “Fabrication and bonding of thiol-ene-based microfluidic devices,” *J. Micromech. Microeng.*, vol. 23, no. 3, p. 037002, 2013.
- [28] S. M. Tähkä, M. E. Nordberg, A. Bonabi, V. P. Jokinen, and T. M. Sikanen, “Characterization of native thiol-ene surface chemistry for microchip electrophoresis and fluorescence detection.” Univeristy of Helsinki. Finland.
- [29] S. S. Shevkoplyas, A. C. Siegel, R. M. Westervelt, M. G. Prentiss, and G. M. Whitesides, “The force acting on a superparamagnetic bead due to an applied magnetic field,” *Lab Chip*, vol. 7, no. 10, pp. 1294–1302, 2007.
- [30] A. H. C. Ng, K. Choi, R. P. Luoma, J. M. Robinson, and A. R. Wheeler, “Digital microfluidic magnetic separation for particle-based immunoassays,” *Anal. Chem.*, vol. 84, no. 20, pp. 8805–8812, 2012.
- [31] J. Wang, K. Morabito, T. Erkers, and A. Tripathi, “Capture and separation of biomolecules using magnetic beads in a simple microfluidic channel without an external flow device,” *Analyst*, vol. 138, no. 21, pp. 6573–6581, 2013.
- [32] “MAGNETIC MICROPARTICLES and NANOPARTICLES - Spherotech.” [Online]. Available: http://www.spherotech.com/para_par.htm. [Accessed: 19-Dec-2014].

- [33] G. C. Papaefthymiou, “Nanoparticle magnetism,” *Nano Today*, vol. 4, no. 5, pp. 438–447, 2009.
- [34] “Dynabeads® M-270 Carboxylic Acid - Life Technologies.” [Online]. Available: <https://www.lifetechnologies.com/order/catalog/product/14305> D. [Accessed: 19-Dec-2014].
- [35] J. Pallares and J. A. Ferré, “A simple model to predict mass transfer rates and kinetics of biochemical and biomedical Michaelis–Menten surface reactions,” *International Journal of Heat and Mass Transfer*, vol. 80, pp. 192–198, 2015.
- [36] S. B. Pope, “PDF methods for turbulent reactive flows,” *Progress in Energy and Combustion Science*, vol. 11, no. 2, pp. 119–192, 1985.
- [37] J. Jeong, F. Hussain, W. Schoppa, and J. Kim, “Coherent structures near the wall in a turbulent channel flow,” *Journal of Fluid Mechanics*, vol. 332, pp. 185–214, 1997.
- [38] “http://msdssearch.dow.com/PublishedLiteratureDOWCOM/dh_0032/0901b803800322b7.pdf?filepath=glycerine/pdfs/noreg/115-00667.pdf&fromPage=GetDoc.” .
- [39] S. N. Kasarova, N. G. Sultanova, and I. D. Nikolov, “Temperature dependence of refractive characteristics of optical plastics,” *J. Phys.: Conf. Ser.*, vol. 253, no. 1, p. 012028, 2010.

- [40] R. J. Adrian, “Scattering particle characteristics and their effect on pulsed laser measurements of fluid flow: speckle velocimetry vs particle image velocimetry,” *Appl. Opt.*, vol. 23, no. 11, pp. 1690–1691, 1984.
- [41] J. Westerweel, F. T. M. Nieuwstadt, TU Delft: Mechanical Maritime and Materials Engineering, and TU Delft, Delft University of Technology, “Digital particle image velocimetry: theory and application.” Delft University Press, 1993.
- [42] J. Westerweel, “Fundamentals of digital particle image velocimetry,” *Measurement Science and Technology*, vol. 8, no. 12, pp. 1379–1392, 1997.
- [43] L. Aanen, *Measurement of Turbulent Scalar Mixing by Means of a Combination of PIV and LIF*. Delft, The Netherlands: DUP Science, 2002.
- [44] S. V. Varela Ballesta, “Computational and experimental modeling of fluid flow and heat transfer processes in complex geometries,” *TDX (Tesis Doctorals en Xarxa)*, 2012. [Online]. Available: <http://www.tdx.cat/handle/10803/80717>. [Accessed: 07-Aug-2014].
- [45] R. J. Adrian, “Twenty years of particle image velocimetry,” *Experiments in Fluids*, vol. 39, no. 2, pp. 159–169, 2005.
- [46] J. Nogueira, A. Lecuona, and P. A. Rodríguez, “Local field correction PIV: on the increase of accuracy of digital PIV

- systems,” *Experiments in Fluids*, vol. 27, no. 2, pp. 107–116, 1999.
- [47] Sylvana Varela, *Flujos cerrados en cilindros y rompimiento de vortices*. Uruguay: Universidad de la República, 2008.
- [48] N. Ertürk, A. Düzgün, J. Ferrè, S. Varela, and A. Vernet, “Alginate flow seeding microparticles for use in Particle Image Velocimetry (PIV).” Delft University of Technology, Faculty of Mechanical, Maritime and Materials Engineering, and Faculty of Aerospace Engineering, 2013.
- [49] M. Bruchhausen, F. Guillard, and F. Lemoine, “Instantaneous measurement of two-dimensional temperature distributions by means of two-color planar laser induced fluorescence (PLIF),” *Exp Fluids*, vol. 38, no. 1, pp. 123–131, 2004.
- [50] D. A. Walker, “A fluorescence technique for measurement of concentration in mixing liquids,” *J. Phys. E: Sci. Instrum.*, vol. 20, no. 2, p. 217, 1987.
- [51] P. S. Karasso and M. G. Mungal, “PLIF measurements in aqueous flows using the Nd: YAG laser,” *Experiments in Fluids*, vol. 23, no. 5, pp. 382–387, 1997.
- [52] S. Komori, T. Kanzaki, and Y. Murakami, “Simultaneous measurements of instantaneous concentrations of two reacting species in a turbulent flow with a rapid reaction,” *Physics of Fluids A*, vol. 3, no. 4, pp. 507–510, 1991.

- [53] P. S. Karasso and M. G. Mungal, “PLIF measurements in aqueous flows using the Nd:YAG laser,” *Experiments in Fluids*, vol. 23, no. 5, pp. 382–387, 1997.
- [54] Y. Hu, Z. Liu, J. Yang, Y. Jin, and Y. Cheng, “Study on the reactive mixing process in an unbaffled stirred tank using planar laser-induced fluorescence (PLIF) technique,” *Chemical Engineering Science*, vol. 65, no. 15, pp. 4511–4518, 2010.
- [55] “FLUENT v14.0 Theory Guide and Users Manual, ANSYS INC.” .
- [56] H. Schlichting, K. Gersten, and K. Gersten, *Boundary-Layer Theory*. Springer Science & Business Media, 2000.
- [57] “Permanent magnet supplier.” [Online]. Available: <http://www.supermagnete.fi/spa/>. [Accessed: 22-Oct-2014].
- [58] “COMSOL - CFD Module: User’s Guide”.
- [59] “COMSOL - AC/DC Module: User’s Guide”.
- [60] “COMSOL - Particle Tracing Module: User’s Guide”.

UNIVERSITAT ROVIRA I VIRGILI

EXPERIMENTAL AND NUMERICAL ANALYSES OF FLOW-LIMITED CHEMICAL REACTIONS IN LAMINAR AND
TURBULENT REGIMES.

Irene Sancho Conde

Dipòsit Legal: T 994-2015

UNIVERSITAT ROVIRA I VIRGILI

EXPERIMENTAL AND NUMERICAL ANALYSES OF FLOW-LIMITED CHEMICAL REACTIONS IN LAMINAR AND
TURBULENT REGIMES.

Irene Sancho Conde

Dipòsit Legal: T 994-2015

UNIVERSITAT ROVIRA I VIRGILI

EXPERIMENTAL AND NUMERICAL ANALYSES OF FLOW-LIMITED CHEMICAL REACTIONS IN LAMINAR AND
TURBULENT REGIMES.

Irene Sancho Conde

Dipòsit Legal: T 994-2015